

^{13}CO IN ORION

K. SUGITANI, Y. FUKUI, H. OGAWA, AND K. KAWABATA

Department of Astrophysics, Nagoya University

Received 1984 December 6; accepted 1985 October 1

ABSTRACT

New $^{13}\text{CO}(J=1-0)$ measurements of the Orion molecular cloud are reported. Data were taken with the new 4 m millimeter-wave telescope of Nagoya University having a beamwidth of $2.7'$. High-velocity resolution of 0.1 km s^{-1} employed has revealed significant details of the ^{13}CO emission toward the H II region. We find that the ^{13}CO emission consists of 14 separate features and the main N-S ridges.

The results indicate that an appreciable portion of the molecular gas toward the Orion nebula is interacting with the H II region. In particular, the molecular gas within about 1 pc of the Trapezium stars appears to be interacting strongly with the H II region. There is evidence for a ^{13}CO cavity of approximately 0.6 pc radius around the Trapezium stars, whose form is fairly anisotropic. The velocity distribution of the material comprising the cavity wall is rather systematic but is as well asymmetric, which does not permit explanation in terms of the uniform expansion of a simple shell.

Outside the central 1 pc of the nebula, ^{13}CO emission is extended in a complicated shape. It seems that a significant portion of the extended ^{13}CO emission is also interacting with the H II region. On the northeast rim of the the nebula, a belt of ^{13}CO emission is likely responsible for the asymmetric expansion of the nebula.

It is not clear if the ^{13}CO features identified represent swept-up material due to the H II region; in some cases, we find that initial inhomogeneities of the undisturbed cloud can better explain the molecular distribution.

We investigate gravitational stability of each ^{13}CO feature by using the virial theorem, taking into account the pressure of the H II region. It is found that most of the ^{13}CO features are nearly in stable equilibrium and that two of the features located at the southern edge of the nebula are gravitationally unstable if their sizes are close to what are observed. These findings are discussed in terms of star formation triggered by H II expansion.

Subject headings: interstellar: molecules — nebulae: H II regions — nebulae: Orion Nebula

I. INTRODUCTION

The Orion Nebula is one of the most prominent nebulae in the sky and has been the subject of a considerable investigation at various wavelengths. The nebula is associated with a massive molecular cloud as revealed by millimeter-wave CO and ^{13}CO observations. Loren (1979) shows that some of the molecular features are explained as being expanding due to dynamical interaction with the H II region. Subsequent CO studies reveal further indications of the interaction (Schloerb, Goldsmith, and Scoville 1982; Goldsmith *et al.* 1982; Schloerb and Loren 1982).

The interaction between an H II region and its ambient molecular gas can be manifold. The radiation emitted by the ionizing stars will heat up the molecular gas, and the high pressure of the H II region will compress the ambient gas via ionization-shock fronts. This compression might further heat up the molecular gas and trigger star formation in the post-shock layer (e.g., Elmegreen and Lada 1977). On the other hand, if the ambient gas is dense enough, the evolution of the H II region may be significantly affected by the ambient gas resulting in an anisotropic expansion (e.g., Tenorio-Tagle 1979; Bodenheimer, Tenorio-Tagle, and York 1979).

These processes can be effectively studied by observing millimeter-wave CO lines. The previous studies mostly use CO transitions ($J=1-0$ or $2-1$), which are optically thick, with relatively low-velocity resolution (in most cases about 0.6 km s^{-1}). Although the CO lines are good tracers of kinetic temperature in so far as self-absorption is not important, it is not

appropriate to use the CO data alone to delineate the molecular gas which is dynamically interacting with the H II region. Because the kinetic temperature is also easily affected by radiative heating due to nearby stars unrelated to the H II region, a column density tracer, ^{13}CO , may be used to better delineate the dynamical interaction. In addition, a high-velocity resolution better than 0.3 km s^{-1} is required in order to resolve the line shape of narrow features, which may arise from the interacting regions. Such an example obtained in the present observations is shown in Figure 1, which presents a $^{13}\text{CO}(J=1-0)$ profile having a line width of 0.9 km s^{-1} toward the periphery of the Orion Nebula. The line width of ^{13}CO emission provides good information on the internal kinematics of molecular gas such as the supporting force in clouds.

In this paper we report the $J=1-0$ data of ^{13}CO and CO in Orion obtained with the new Nagoya 4 m millimeter-wave telescope in conjunction with a spectrometer having 0.1 km s^{-1} spectral resolution. We emphasize the presentation of detailed kinematical characteristics and spatial distribution of the molecular features which may be interacting with the H II region, although some of the features have been discussed previously qualitatively and on an individual basis. In addition, we investigate gravitational stability of the ^{13}CO features.

II. OBSERVATIONS

Observations were made with the 4 m millimeter-wave telescope of Department of Astrophysics, Nagoya University.

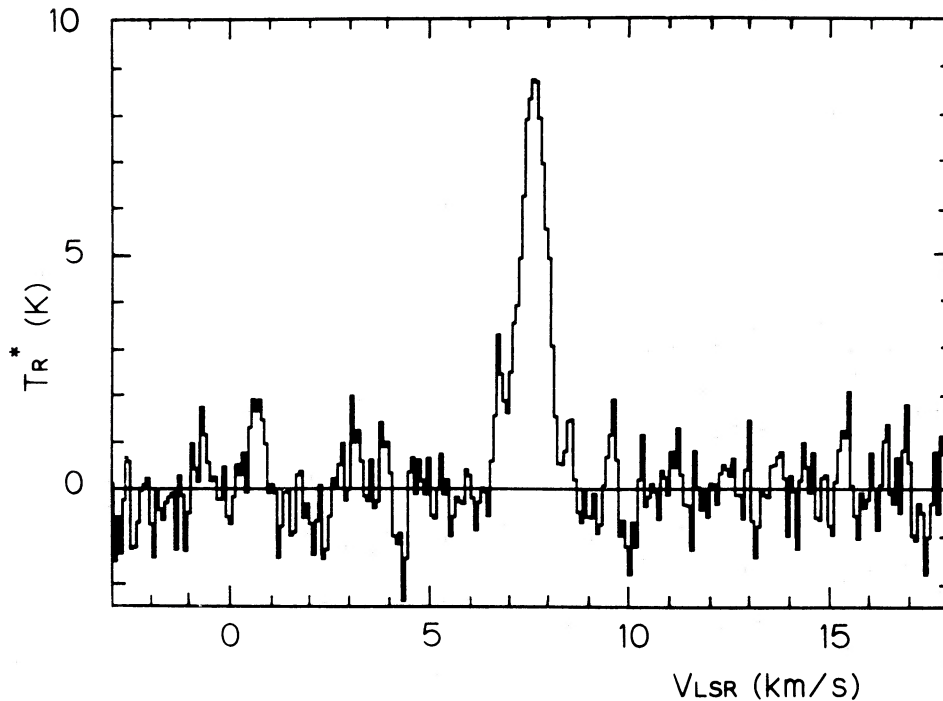


FIG. 1.—A $^{13}\text{CO}(J=1-0)$ profile obtained toward the periphery of the Orion Nebula in the present observations: R.A. $5^{\text{h}}33^{\text{m}}23^{\text{s}}$; decl. $-5^{\circ}34'50''$

Details of the telescope are described by Kawabata *et al.* (1985). The CO data were obtained in 1983 December and 1984 February with a room temperature receiver whose system noise temperature was around 500 K (DSB). The ^{13}CO data were taken in 1984 April and May with a 15 K cooled mixer receiver whose noise temperature was 200 K (DSB). Spectral data were taken with an acousto-optical spectrometer having 40 kHz frequency resolution and 40 MHz bandwidth, which gave a velocity resolution of 0.1 km s^{-1} and a velocity coverage of 110 km s^{-1} at 2.7 mm wavelength (Takano *et al.* 1983). Observations were mostly made by frequency switching 13 MHz ($=35 \text{ km s}^{-1}$ at 2.7 mm). The CO spectrum toward Orion KL was observed by position switching due to the high-velocity CO wing. The spectral intensity was calibrated by observing an ambient temperature load relative to blank sky and then normalized by referring to the KL object whose $T_R^*(\text{CO})$ and $T_R^*(^{13}\text{CO})$ are assumed to be 70 K and 10 K, respectively. During the observing period we observed the KL object every hour or so, and the peak-to-peak relative calibration uncertainty is less than 10%.

The half-power beamwidth of the 4 m telescope was measured to be $2.7'$ at 2.7 mm, and the pointing accuracy was better than $15''$ rms. The beam efficiency for the solar disk was measured to be 0.77, while the main beam efficiency estimated from the response to the solar rim was 0.71. Therefore, more than 90% of the forward power is contained within the main beam when mapping CO clouds having sizes of $\lesssim 30'$.

The mapped area is about $30'$ in R.A. by 1° in decl. centered near the Trapezium stars and the KL object. The center of mapping is R.A. = $5^{\text{h}}32^{\text{m}}47.0^{\text{s}}$ and decl. = $-5^{\circ}25'50''$ (1950.0). ^{13}CO spectra were sampled with a $1.5'$ grid spacing in the inner part and with a $3'$ spacing elsewhere, while CO spectra were taken with a $3'$ spacing. The numbers of the ^{13}CO and CO spectra are approximately 400 and 200, respectively. In this paper we focus on the ^{13}CO data. CO data are used for deriving the molecular mass listed in Table 2.

III. RESULTS

In Figures 2 and 3, we present maps of peak and integrated intensities of ^{13}CO . The most prominent structure is the elongated ridge by about 1° in length ($\sim 9 \text{ pc}$ at the distance of $\sim 500 \text{ pc}$) in the north-south direction. The east-west width of the ridge is about $15'$ ($\sim 2 \text{ pc}$). The brightest part of ^{13}CO in Figures 2 and 3 is located within $4'$ of the map center, indicating close association of the brightest part to the region of the Trapezium stars and the KL/BN infrared objects. Away to the east and west from the ridge, weak emission is extended at the intensity levels of 1.5 K to 6 K in the peak intensity or of 2.5 K km s^{-1} to 10.0 K km s^{-1} in the integrated intensity. The locations of the extended emission are $\Delta\text{R.A.} \gtrsim 4.5\text{E}$ and $24'\text{S} \lesssim \Delta\text{decl.} \lesssim 6'\text{N}$ on the east and $\Delta\text{R.A.} \lesssim 4.5\text{W}$ and $18'\text{S} \lesssim \Delta\text{decl.} \lesssim 15'\text{N}$ on the west. In this section, we describe the ^{13}CO data for the brightest part and for the extended part, respectively.

In Figures 2 and 3, the ^{13}CO distribution seems rather continuous, but the maps at individual velocities indicate that the ^{13}CO emission consists of discrete features of different velocities. We have identified 14 ^{13}CO features in equivelocity maps constructed every 0.5 km s^{-1} . These ^{13}CO features are listed in Table 1 along with the comparison with known optical features and with the previously noticed CO features.

a) Brightest Part of the ^{13}CO Emission within 1 Parsec of Trapezium Stars

We identify four features, C1–C4, in the brightest part of the ^{13}CO emission. They are schematically shown in Figure 5. For presenting the kinematics and distribution of the ^{13}CO emission near the map center in detail, we give integrated intensity maps for the central $15' \times 15'$ region every 0.5 km s^{-1} in Figure 4. The ^{13}CO emission is mostly found between 6.0 and 13.0 km s^{-1} . At the low velocities around 7.0 km s^{-1} , a single cloud appears at (1.5W, 0') (hereafter positions are given as the

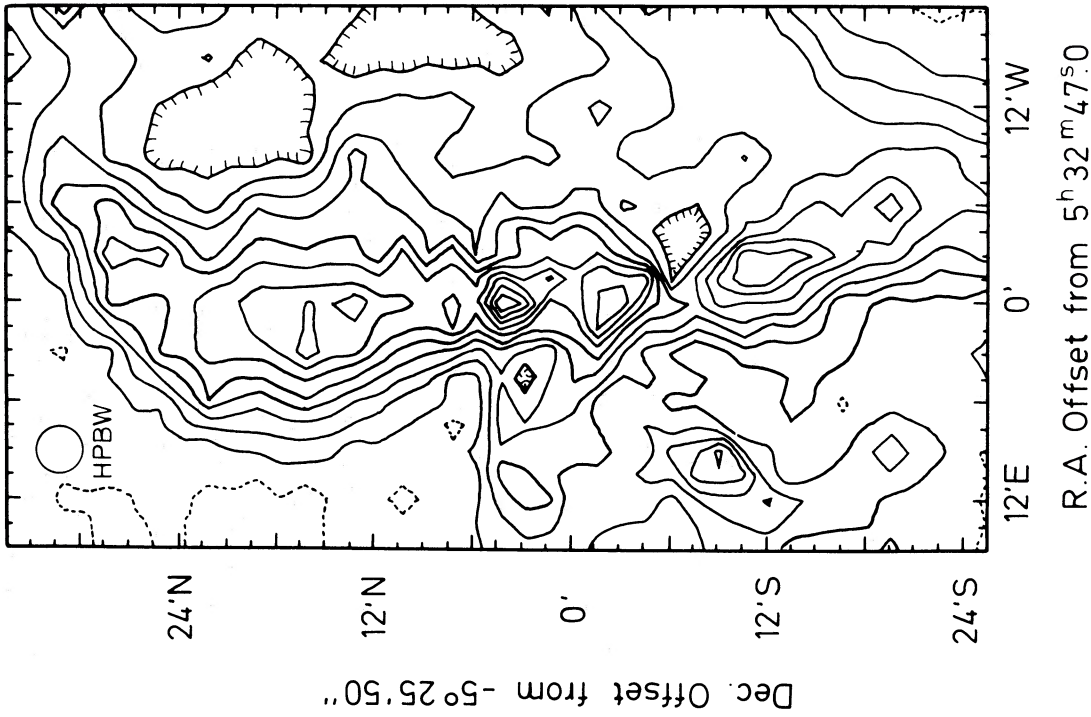


FIG. 2

FIG. 2.—Distribution of the peak intensity of $^{13}\text{CO}(J = 1-0)$ line radiation in the Orion molecular cloud. The contour unit and the lowest contour (*dotted line*) are 1.5 K in T_R^* . The half-power beam size is $2.7''$.

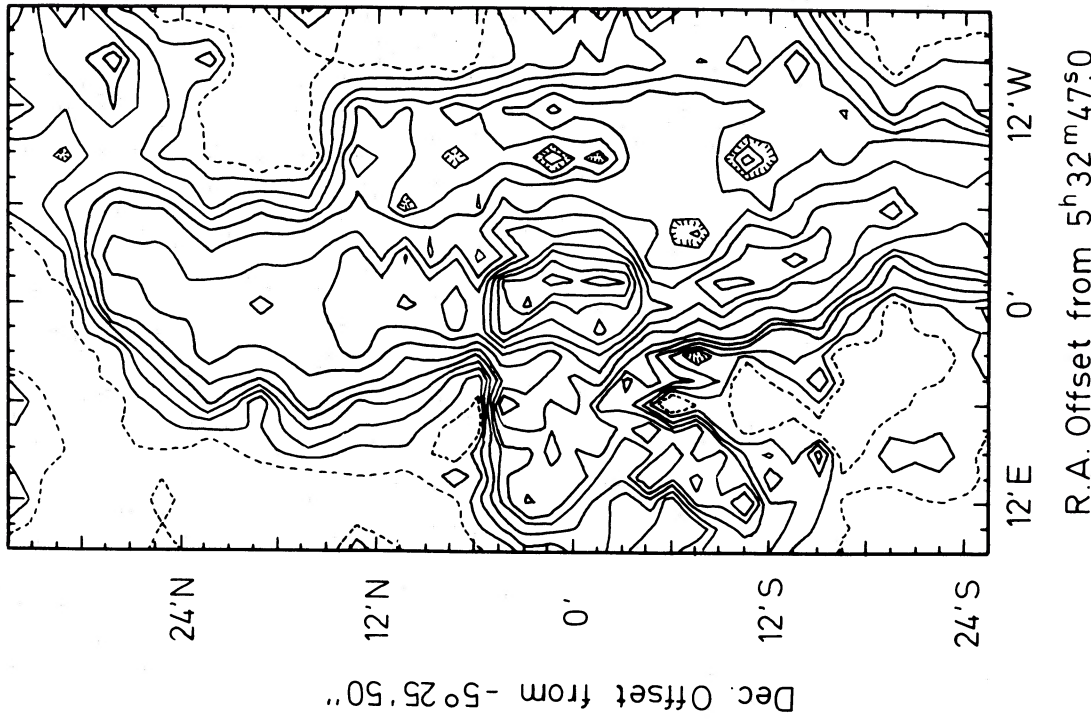


FIG. 3

FIG. 3.—Distribution of the total integrated intensity of ^{13}CO line radiation. The integration range in V_{LSR} is from 4.5 to 14.5 km s^{-1} . The lowest six contours are every 2.5 K km s^{-1} with the lowest contour (*dotted line*) being 2.5 K km s^{-1} . The other contours are every 5 K km s^{-1} .

TABLE 1
SUMMARY OF THE ^{13}CO FEATURES

Feature	Position ($\Delta\text{R.A.}, \Delta\text{decl.}$)	V_{LSR} (km s^{-1})	Remarks	References
C1	(1'5W, 1'5N)	6.0–8.5	No optical features	1
C2	(0', 1'5S)	9.0–10.5	[S II] streamers	1
C3	(1'5E, 1'5S) (1'5W, 3'S)	7.5–11.5	The bright bar	1
C4	(3'W, 1'5S)	11.0–13.0	No optical features	2, 3 (part of feature 8)
E1	(0', 7'5S)	5.5–6.5	No optical features	2, 4, 5
E2	(4'5E, 4'5N)	6.5–8.5	Near the dark bay	3 (feature 4)
E3	(9'E, 9'S)	6.5–8.5	East rim of the optical nebula	3 (feature 5)
E4	(4'5W, 3'N)	7.5–9.5	North rim of the optical nebula	3
E5	(12'E, 1'5N)	8.5–10.5	No optical features	3 (feature 6)
E6	(0', 15'S)	9.5–10.5	No optical features	2
E7	(6'W, 13'5N)	10.5–12.5	No optical features	2
E8	(6'E, 1'5N)	10.5–13.5	East rim of the optical nebula	3 (feature 7)
West Rim	(12'W, 0')	7.5–11.5	[S II] west rim	2, 3
West Protrusion	(\lesssim 4'5W, 12'S–0')	6.5–10.5	No optical rim, similar velocity components in [N II] emission	2

REFERENCES.—(1) Schloerb, Goldsmith, and Scoville 1982. (2) This work. (3) Loren 1979. (4) Goldsmith *et al.* 1982. (5) Schloerb and Loren 1982.

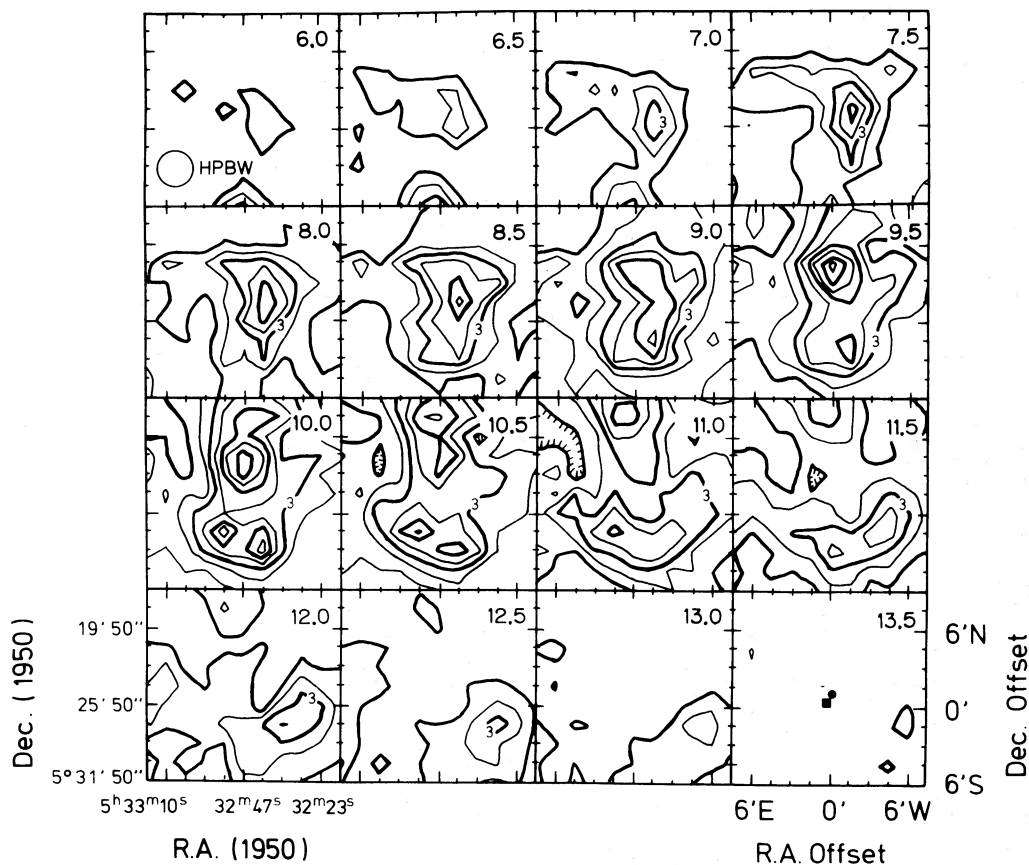


FIG. 4.—Integrated intensity maps of ^{13}CO every 0.5 km s^{-1} in V_{LSR} . The map is sampled every $1.5'$. Contour unit is 1 K km s^{-1} . The positions of the KL/BN objects and the Trapezium stars are denoted by filled circles and filled squares, respectively.

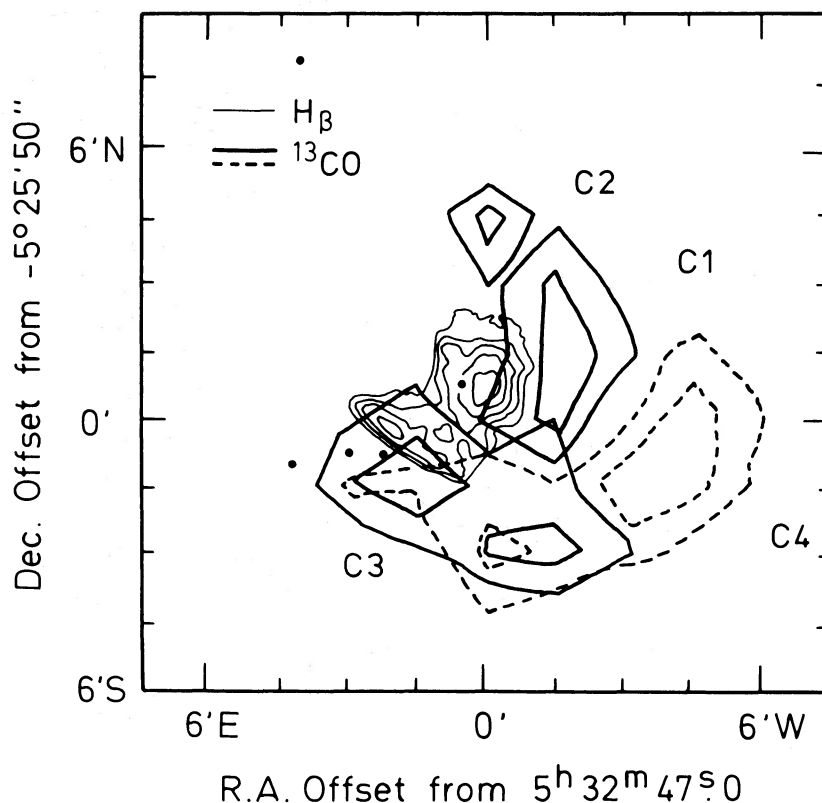


FIG. 5.—A schematic drawing of the typical ^{13}CO peaks in Fig. 4. Also reproduced is the brightest part of the $\text{H}\beta$ emission (Dopita, Isobe, and Meaburn 1975). The central velocities of the ^{13}CO features C1–C4 are 8.0, 9.8, 10.0, and 11.5 km s^{-1} , respectively.

offsets in R.A. and decl. from the map center) and at the intermediate velocities of 9.0–10.0 km s^{-1} , the cloud appears to split into two components which have peaks at (0', 4.5N) and (1.5W, 1.5S), respectively. At the high velocities of $\sim 11.0 \text{ km s}^{-1}$, an arc-like structure appears on the south of the center, which is most evident at 11.0 km s^{-1} (see Fig. 4). The velocity variations occur rather systematically. The features found in Figure 4 are basically similar to the $\text{CO}(J = 1-0)$ maps at three V_{LSR} , 6.5, 8.5, and 10.5 km s^{-1} (Schloerb, Goldsmith, and Scoville 1982). The present data show that the manner of velocity variation in the features is fairly continuous even at the velocity intervals of 0.5 km s^{-1} .

Three of these ^{13}CO features, C1, C2, and C3, are located adjacent to the rim of the brightest part of the $\text{H}\beta$ emission around the Trapezium stars as seen in Figure 5. C1 lies on the west of the brightest part of the $\text{H}\beta$ emission. The eastern half of the arc-like structure, C3, is associated with the optical bright bar as previously noticed in the $\text{CO}(J = 1-0)$ map taken with a 50" beam (Schloerb, Goldsmith, and Scoville 1982).¹ The bar feature of ^{13}CO is more extended toward the southwest than the optical bright bar, where faint [S II] emission is observed (Gull 1974) and has two peaks at (1.5W, 3'S) and (1.5E, 1.5S). The western half of the arc-like structure, C4, is not seen in the $\text{CO}(J = 1-0)$ map and is apparent only in the $^{13}\text{CO}(J = 1-0)$ map. C4 is elongated on the west of the center similarly to C3

with respect to the Trapezium stars and occurs toward the region of much weaker $\text{H}\beta$ emission than the bright bar. C4 is redshifted up to about 13 km s^{-1} , and its location shifts monotonically toward the southwest with velocity as noticed on panels from 11.0 km s^{-1} to 13.0 km s^{-1} in Figure 4, indicating a velocity gradient orthogonal to the elongation.

For presenting more details about the kinematics which are not readily seen in Figure 4, we show a few spatial velocity maps in Figure 6. Figure 6a shows a velocity-declination cut at 1.5W of the center. A systematic velocity variation of the intensity peaks is seen. We find ^{13}CO emission extends down to 5.5 km s^{-1} at $\Delta\text{decl.} = 0'$ and up to 13 km s^{-1} at $\Delta\text{decl.} = 4.5\text{S}$. A velocity-right ascension cut at 1.5S of the center is shown in Figure 6b. We find an abrupt velocity jump at 1.5W in right ascension, which indicates that the arc-like structure consists of two components of different velocities, C3 and C4, and a large relative blueshift down to about 5 km s^{-1} at $\Delta\text{R.A.} = 0'$. In Figure 6c, we show a velocity-position cut along the bright bar feature, i.e., in the northeast-southwest direction. The velocity distribution is rather systematic and is asymmetric. The line width, for instance, decreases monotonically from about 6 km s^{-1} to about 2 km s^{-1} at the fourth lowest contour level in Figure 6c, and most of the emission is significantly blueshifted relative to the peak velocity at $\sim 10.3 \text{ km s}^{-1}$, which remains uniform.

b) Extended ^{13}CO Emission

Detailed description of the individual features in the extended ^{13}CO emission is given in the Appendix. We refer to these features as E1–E8, the West Protrusions, and the West Rim (see Table 1). They are schematically shown in Figure 7.

¹ The bright bar feature, C3, is not seen in the previous $\text{CO}(J = 1-0)$ and $^{13}\text{CO}(J = 1-0)$ maps taken with a beam size of 2.3 of the Texas 4.9 m telescope (Schloerb and Loren 1982). This might be partly ascribed to the higher velocity resolution of the present spectrometer because the beam efficiencies of the two telescopes are very similar (Kawabata *et al.* 1985).

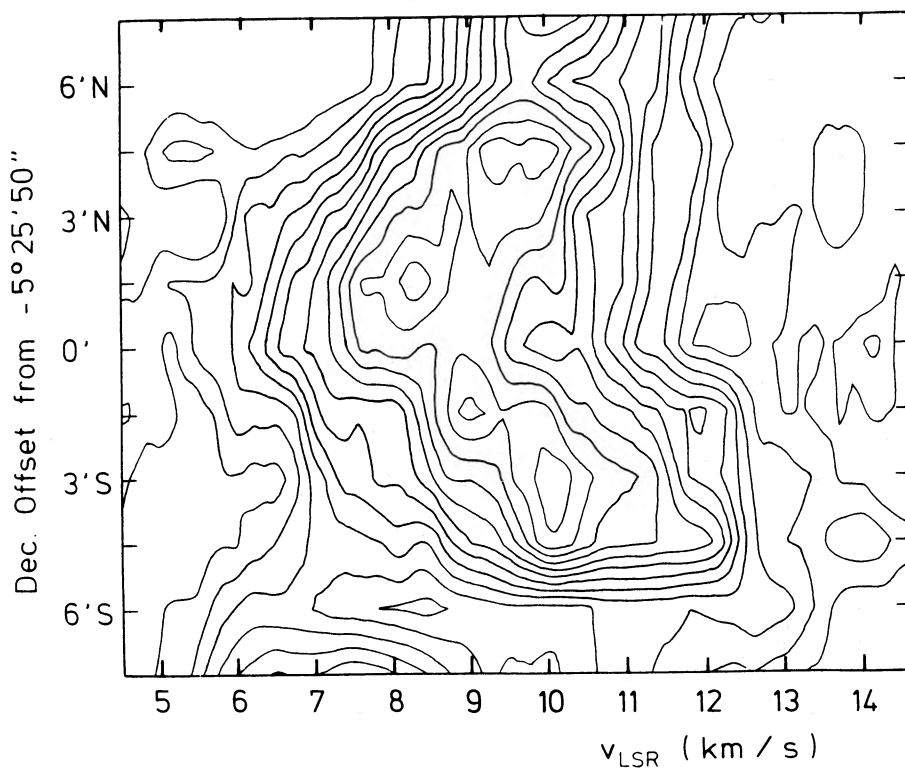


FIG. 6a

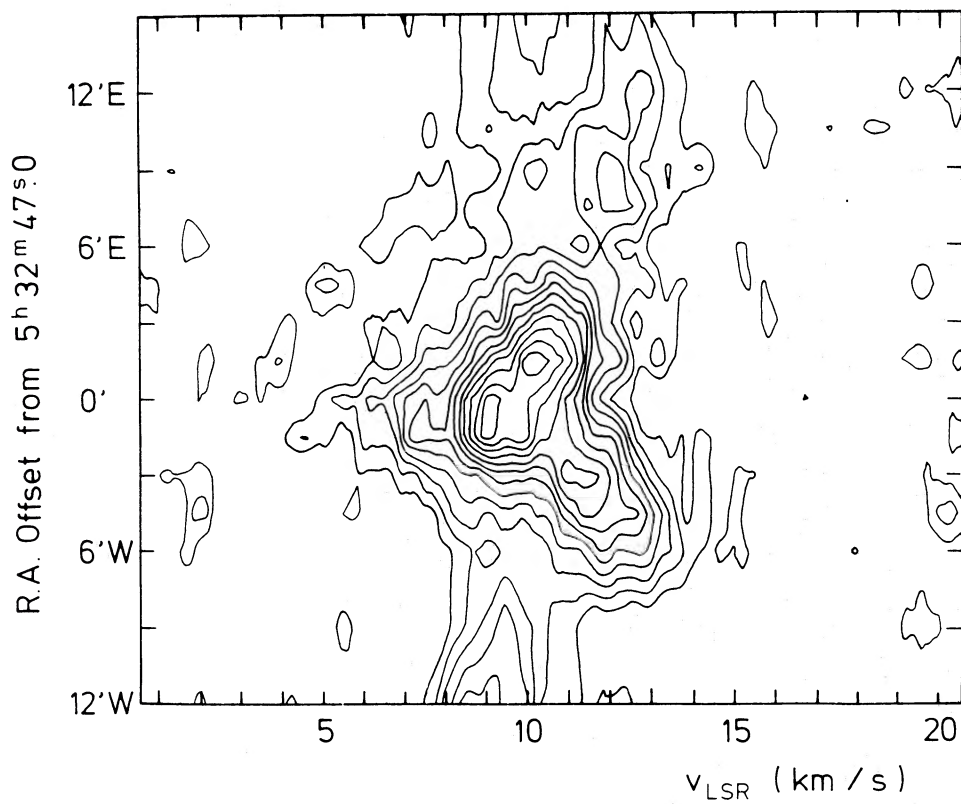


FIG. 6b

FIG. 6.—Velocity-position maps of the brightest part of the ^{13}CO emission. Contour unit and the lowest contour are 1 K. (a) R.A. = $5^{\text{h}}32^{\text{m}}41^{\text{s}}$. (b) Decl. = $-5^{\circ}27'20''$. (c) Bright Bar (NE-SW).

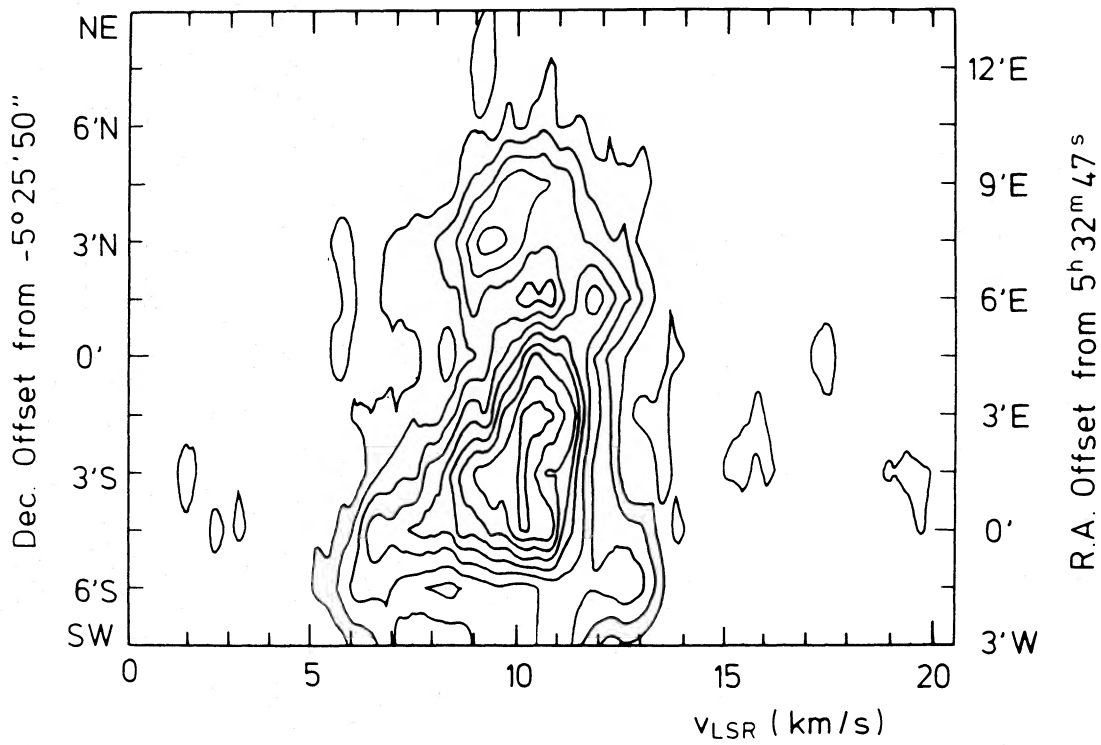


FIG. 6c

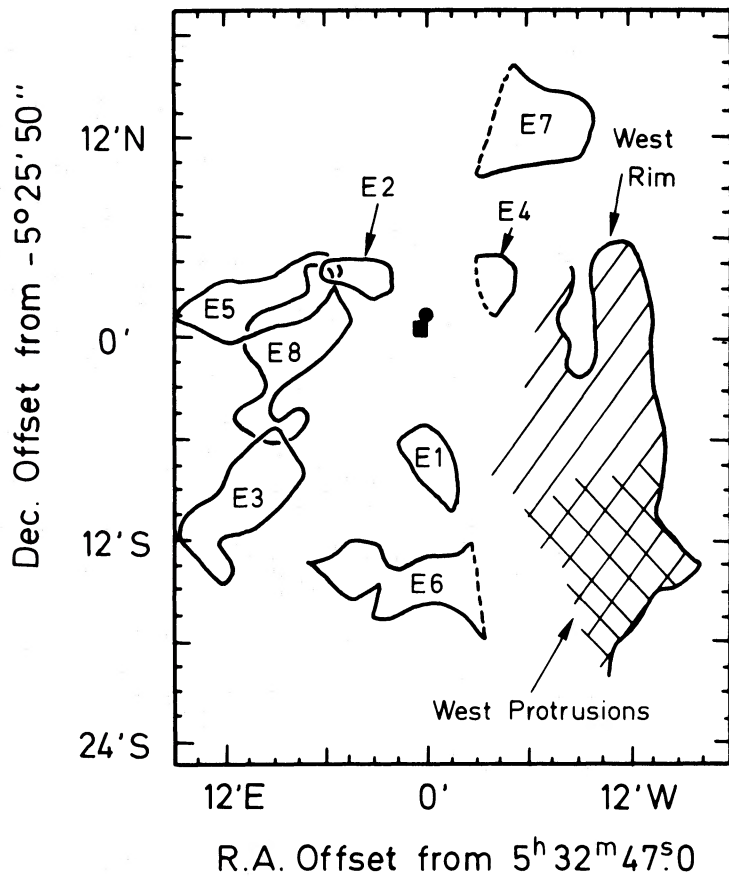


FIG. 7.—A schematic diagram of the ^{13}CO features identified in the text. The position of the KL/BN object and the Trapezium are shown by a filled circle and a filled square, respectively.

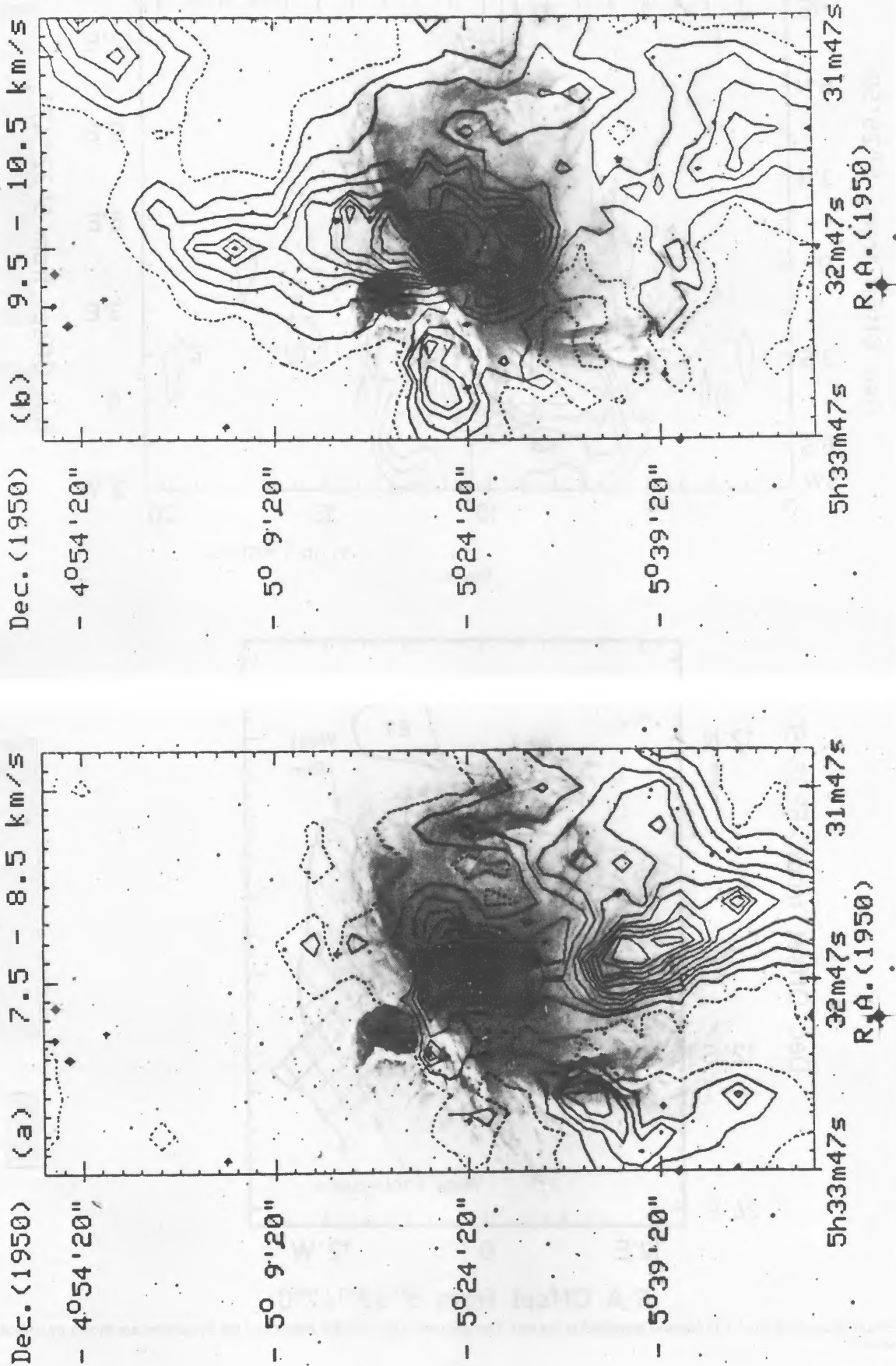


FIG. 8.—Integrated intensity maps of $^{13}\text{CO}(J = 1-0)$. Contour interval and the lowest contour are 1 K km s^{-1} . The velocity ranges of integration are (a) $7.5-8.5 \text{ km s}^{-1}$, (b) $9.5-10.5 \text{ km s}^{-1}$, (c) $10.5-11.5 \text{ km s}^{-1}$, and (d) $11.5-12.5 \text{ km s}^{-1}$, respectively. (a), (b), and (d) are superposed on a photograph of Hz emission taken at the Kiso Observatory.

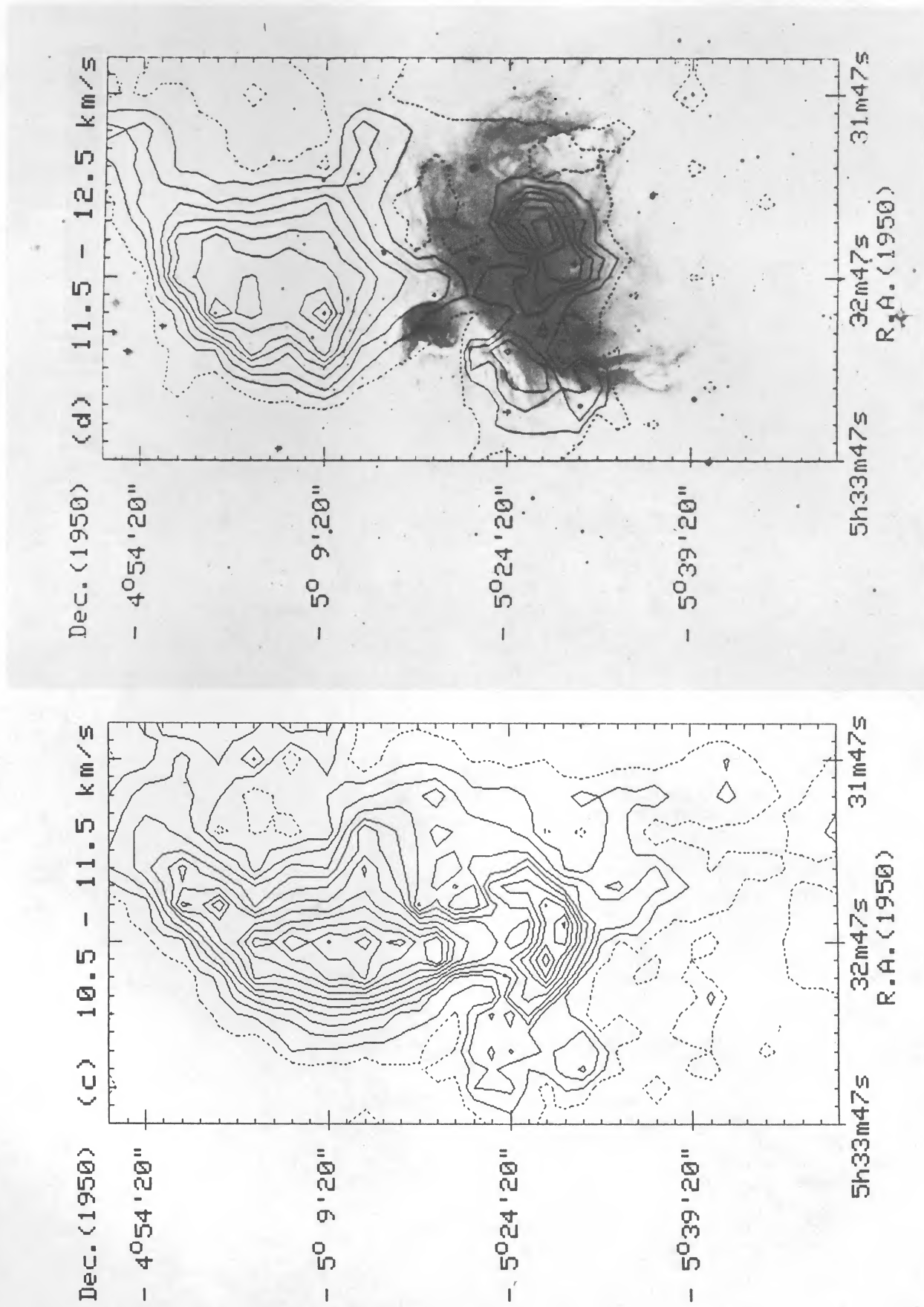


FIG. 8—Continued

TABLE 2
SUMMARY OF THE PHYSICAL PARAMETERS OF THE ^{13}CO FEATURES

Feature	$T_R^*(\text{CO})$ (K)	$T_R^*(^{13}\text{CO})$ (K)	$\tau(^{13}\text{CO})$	$V_{\text{LSR}}(^{13}\text{CO})^a$ (km s^{-1})	Δv^b (km s^{-1})	$N(\text{H}_2)$ ($\times 10^{22} \text{ cm}^{-2}$)	Size (pc)	Mass (M_\odot)
C1	33	12	0.45	8.0	2.6	3.8	1.3×0.7	360
C2	45	15	0.40	9.8	2.0	4.6	1.4×0.8	460
C3	60	13	0.24	10.0	3.0	7.0	1.3×0.7	700
C4	18	7	0.49	11.5	2.0	1.2	1.3×0.6	100
Total (C1–C4)	1620
E1	20	6	0.36	6.0	1.5	0.75	0.8×0.5	30
E2	20	4	0.22	7.5	1.7	0.53	0.8×0.6	26
E3	30	9	0.36	7.5	0.9	0.89	1.3×0.6	81
E4	25	8	0.38	8.5	1.9	1.5	0.6×0.4	39
E5	27	5	0.20	9.5	2.0	0.94	1.4×0.6	86
E6	18	3	0.18	10.0	1.2	0.25	1.4×0.6	25
E7	24	7	0.34	11.0	1.7	1.1	1.0×1.0	120
E8	30	5	0.18	12.0	2.3	1.1	1.5×0.4	140
EE ^c	12–20	3–6	≥ 300
Total (E1–EE)	≥ 847

^a Peak velocity of ^{13}CO profiles.

^b Line width at half-intensity.

^c EE: West Rim and West Protrusions.

Some of the ^{13}CO features correspond well to optical features as seen in Figures 8a, 8b, and 8d. They are E2, E3, E5, E8, and the West Rim. Features E2, E3, E5, and E8 are located toward the dark region just beyond the sharp edge of the emission nebula (see Figs. 8a, 8b, and 8d). They are likely located at the interface with the H II region. The west rim feature is seen toward [S II] filaments (Gull 1974) and is probably associated with the shock front in which the [S II] line is emitted. Because the west rim feature does not well correspond to any optical dark area, the molecular gas probably lies behind the [S II] emitting gas. Most of the other ^{13}CO features may be in contact with the H II region, although the association becomes less clearly seen than in cases of E2, E3, E5, and E8. Only an exception is E7 which lies more than $4'$ separated from the nebula. Therefore, E7 is unlikely in contact with the H II region.

IV. PHYSICAL PARAMETERS OF THE ^{13}CO FEATURES

We calculate physical parameters of the ^{13}CO features identified in § III. We use the $J = 1-0$ CO and ^{13}CO data for estimating the molecular column density by using the LTE approximation. Conversion of the ^{13}CO column density to the H_2 column density is made by using the ratio 5×10^5 (Dickman 1978). Major and minor diameters of each ^{13}CO feature are determined at the half-intensity level. Derived parameters are listed in Table 2. In Table 2, we find that the peak ^{13}CO optical depth is less than 0.5 indicating that saturation effect is not important in the ^{13}CO line. Features C1–C3 have large $N(\text{H}_2)$ of $4-7 \times 10^{22} \text{ cm}^{-2}$ and mass of 360–700 M_\odot . The features in the extended emission and C4 have smaller $N(\text{H}_2)$ of $0.2-1.5 \times 10^{22} \text{ cm}^{-2}$ and mass of 26–140 M_\odot . The total molecular mass for C1–C4 and E1–EE amounts to $\sim 2500 M_\odot$. This is comparable to that of the main N-S ridge, $\sim 3000 M_\odot$.

We estimate the kinetic energy for the ^{13}CO features and the mutual gravitational energy for C1–C4. LSR velocities are projected to the line of sight and are lower limits to actual velocities. Therefore, the kinetic energy estimated here is a lower limit. Similarly, distances among C1–C4 are lower limits to

actual separations and the gravitational potential energy estimated gives an upper limit. The results are summarized in Table 3. We find that C1–C4 have kinetic energy of 10^{45} – 10^{46} ergs individually and that the gravitational energy of C1–C4 is roughly the same with the sum of their kinetic energy. We note that contribution of the stellar mass to the gravitational energy does not significantly affect this estimate (Blaauw 1964).

V. MOLECULAR GAS AND THE H II REGION

a) The ^{13}CO Features in the Vicinity of the Trapezium Stars: A Cavity Created by the H II Region

We have shown that ^{13}CO features within 1 pc of the Trapezium stars show close association with the optical nebula. Recent radio continuum observations of the H II region reveal detailed distribution of the ionized gas, which is very similar to

TABLE 3
ENERGY ESTIMATE OF THE ^{13}CO FEATURES

Feature	Lower Limit for Kinetic Energy ^a ($\times 10^{45}$ ergs)	Upper Limit for Gravitational Energy ($\times 10^{45}$ ergs)
C1	3.6	...
C2	2.9	...
C3	7.0	...
C4	6.3	...
Total (C1–C4)	19.8	11.0 ^b
E1	2.7	...
E2	0.59	...
E3	1.8	...
E4	0.01	...
E5	0.22	...
E6	0.25	...
E7	4.8	...
E8	12.6	...
Total (E1–E8)	23.1	...

^a Kinetic energy of each ^{13}CO feature estimated by taking the central velocity of gravity to be 9 km s^{-1} .

^b Total mutual gravitational energy of C1, C2, C3, and C4.

that of the optical emission (Johnston *et al.* 1983; Wilson and Pauls 1984; Akabane *et al.* 1985). In the following, we shall make a detailed comparison of spatial distribution between the molecular and ionized gas.

The distributions of both the radio continuum and optical indicate that the high density ionized gas is distributed very anisotropically with respect to the Trapezium stars and that there are sharp intensity gradients toward the west and the southeast (see, e.g., Fig. 5). The brightest part of the molecular distribution appears to embrace the brightest part of the H II region, suggesting that the ionized region is partially surrounded by the molecular layer of enhanced column density. Among the four ^{13}CO features, we find that particularly C1 and C3 are remarkably well correlated with the sharp gradients of the H II region. The interaction is even more evidenced by the following optical features; for C3 the bright bar feature of [S II] and for C1 "[S II] streamers" extending toward the west (Gull 1974). Features C1, C2, and C3 are apparent also in a CO($J = 1-0$) map (Schloerb, Goldsmith, and Scoville 1982), and the authors suggest that the high CO intensities are due to heating by the H II region. The present data indicate that C1, C2, and C3 are also features with highest molecular column densities in the Orion region. Feature C4, which is apparent in ^{13}CO but not so in CO, is not in contact with the brightest part of the H II region. This separation might explain its low CO intensity (see Table 2).

The present ^{13}CO distribution seems well explained by the model which has a cup-shaped eroded region in the molecular cloud (Pankonin, Walmsley, and Harwit 1979; Jaffe and Pankonin 1978). The present data indicate evidence for such a cavity-like structure around the Trapezium stars which appears as the high ^{13}CO brightness region. The distribution, however, is far from isotropic with respect to the Trapezium stars and appears segmentary as seen by features C1–C4. The radius of the cavity is approximately 0.6 pc.

b) Kinematics of the Cavity

It is interesting to ask if the expansion of the H II region has any significant influence on the kinematics and density distribution of the ambient molecular gas. The total kinetic energy of C1–C4 is nearly comparable to, or slightly greater than, their gravitational potential energy as shown in Table 3. Therefore, from the point of view of the virial theorem, there is no strong need for additional source of energy for explaining the motion of the molecular gas. This implies that the motion of the molecular gas within 1 pc of the Trapezium stars is explicable as pre-existent before the disturbance due to the H II region. Nevertheless, the present data suggest that some of the kinematics of the ^{13}CO features, C1, C2, and C3, can be better explained as caused by the dynamical influence of the H II region. In fact, the manner of velocity variation of C1 and C2 is very systematic. The velocity distribution of C3 is systematic and asymmetric with no apparent center of the velocity distribution, although C3, which appears strongly interacting with the H II region, has no concentration of mass like the KL/BN objects. These kinematic properties are probably well explained as due to the influence of the H II expansion. Feature C4 has an elongation similar to C3 with respect to the Trapezium stars and has a velocity gradient orthogonal to its elongation. The kinematics of C4 is better explicable as due to the expansion of the H II region than equilibrium rotation, because the velocity gradient is orthogonal to the elongation.

We suggest that the initial undisturbed gas distribution

around the Trapezium stars was fairly anisotropic because the ^{13}CO distribution is quite asymmetric with respect to the Trapezium stars; i.e., there is no concentration of molecular gas comparable to C1 to the east of the Trapezium stars. The asymmetry is more likely due to initial gas distribution of the undisturbed molecular gas rather than material compressed by the H II expansion. As well, we suggest that initial inhomogeneities have probably played an important role in determining the present segmentary molecular distribution, although the interaction with the H II region can cause additional enhancement of column density. Higher angular resolution ^{13}CO studies, for instance, should be of interest for investigating how the interaction with the H II region affects the enhancement of molecular column density in C1–C4.

It is tempting to speculate on the location of each ^{13}CO feature *when we assume that they are expanding as a result of interaction with the H II region*. Because C1 shows a blueshifted velocity relative to its surroundings by $\sim 2 \text{ km s}^{-1}$, it can be placed on the near side of the H II region if C1 is expanding. Although toward this position there is no clear indication of obscuring matter, we suggest that the VLA data of the 6 cm H_2CO line show a feature similar to C1 in absorption at V_{LSR} about 8 km s^{-1} (Johnston *et al.* 1983). The continuum radiation being absorbed cannot be only the cosmic background radiation, and some of the radio continuum source should lie behind C1 (Johnston *et al.* 1983). A possibility is that C1 is in the H II region as suggested by Wilson and Pauls (1984). The redshifted velocities of C3 and C4 suggest that the two features are on the far side of the H II region.

c) The Extended ^{13}CO Emission

A significant portion of the extended ^{13}CO emission represents molecular gas interacting with the H II region as suggested by the morphology of the molecular gas, its association with [S II] filaments, and its spatial correlation with the optical nebula: strong evidence has been present for E3, E5, E8, and the West Rim. It is, however, not obvious if they represent initial inhomogeneities of the undisturbed gas or largely swept-up material due to the H II expansion. What the present data suggest is that there is molecular material far from the CO main ridge, like E7, which shows no indications of interaction with the H II region. This feature indicates that influence of the H II region is not necessary to explain its separation from the main ridge and may argue for that the molecular distribution seen at present basically represents a preexisting one. This suggestion, of course, does not exclude the possibility of additional compression and acceleration due to the H II region.

In Figures 7 and 8, we notice that the northeast rim of the nebula is almost continuously faced by the ^{13}CO features, E2, E3, E4, E5, and E8, whose total mass is $\sim 370 M_{\odot}$. This suggests that the nebula is actually bordered by the molecular gas in that direction. The expansion of the nebula is highly asymmetric with respect to the ionizing source, the Trapezium stars, and these ^{13}CO features may account for this shape of the nebula as a result of halting the H II expansion.

The ^{13}CO distribution on the west is more complicated and cannot be grasped in a straightforward manner. The ^{13}CO emission is weak and ranges over 6 km s^{-1} on the western side of the main ridge (Table 1; see also Fig. 8). The large spread in velocity suggests that the ^{13}CO features originate in molecular gas which is moving into various directions. The H II expansion can be a good source of kinetic energy for the motion. The molecular distribution may be sheetlike or filamentary as sug-

gested from the broken morphology of the [S II] filaments (see Gull 1974). The total molecular mass estimated for the western features is $\gtrsim 300 M_{\odot}$.

In the above, we have discussed dynamical interaction between the molecular gas and the H II region. This does not necessarily imply that the molecular condensations are swept-up material produced by the H II region. It is also likely that most of the molecular distribution represents more or less the initial density inhomogeneities in the molecular gas, and the H II expansion has occurred so as to follow the initial density gradient of the molecular gas. Even when we can detect emission from proper shock tracers like the far-infrared CO transitions (e.g., Draine and Roberge 1984), the detection implies only that the emitting gas is being shocked and tells nothing about the past history of the associated molecular features.

VI. GRAVITATIONAL STABILITY OF THE ^{13}CO FEATURES

a) Analysis

It is interesting to ask if the ^{13}CO features can lead to star formation as a result of gravitational instability. Here, we investigate the gravitational stability of the ^{13}CO features by applying the virial theorem to the physical parameters derived from the CO and ^{13}CO data.

A stable configuration of a molecular cloud is required to satisfy the virial theorem (e.g., eq. [11-24], Spitzer 1978), which demands that the energy relating to contracting forces is balanced with that relating to supporting forces. For the moment, we assume that the supporting force is due to turbulent and thermal motions and neglect the other effects. This assumption may not be valid for some of the ^{13}CO features and other types of supporting forces like magnetic pressure or centrifugal force due to rotation may exist. Nevertheless, these other effects would not seriously alter the following conclusions as discussed later. The magnitude of turbulence can be estimated from the ^{13}CO line width by subtracting the contribution of thermal broadening that is inferred from the gas kinetic temperature, as long as the ^{13}CO line is not broadened by saturation. The supporting force, which appears in the virial theorem, is then caused by turbulent and thermal motions, and is estimated from the ^{13}CO line width. The supporting force can be

expressed in terms of the equivalent temperature defined by the following equation;

$$T_{\text{eq}} = m(\Delta v)^2/k(8 \ln 2), \quad (1)$$

where m is the mean molecular weight and Δv is the ^{13}CO line width. T_{eq} of each ^{13}CO feature is listed in Table 4. In most cases, the equivalent temperature is significantly greater than the kinetic temperature. On the other hand, the forces contracting the cloud are self-gravity and external pressure in the present case. Because most of the ^{13}CO features are likely faced by the H II region, we adopt the pressure of the H II region as the external pressure exerted on the molecular cloud.

We assume, for simplicity, that each ^{13}CO feature is an isothermal uniform sphere of radius R surrounded by uniform H II gas, and investigate if the observed parameters of the ^{13}CO features satisfy the equilibrium condition. If there are equilibrium solutions, we further inquire if the equilibrium is stable or not. For a cloud of mass M , the condition for the existence of any equilibrium solution is given as follows:

$$P_{\text{ext}} \lesssim P_{\text{ext, max}} = 4.5 \times 10^{21} (T/R)^2 \text{ dyn cm}^{-2}. \quad (2)$$

This relation is derived from equation (11-25) of Spitzer (1978) and indicates that the external pressure at R should be less than $P_{\text{ext, max}}$ for equilibrium. When the actual external pressure P_{ext} is greater than $P_{\text{ext, max}}$, no equilibrium solution exists. If relation (2) is satisfied, the stability of the equilibrium is tested by the relation,

$$N(\text{H}_2) \lesssim N_{\text{max}}(\text{H}_2) = 2.0 \times 10^{38} (T/R) \text{ mol cm}^{-2}. \quad (3)$$

In case $N(\text{H}_2)$ is greater than $N_{\text{max}}(\text{H}_2)$, the equilibrium is unstable, and vice versa. We note that the present analysis is essentially the same with the stability analysis developed by Elmegreen and Lada (1977) for a plane parallel geometry: if $2R$ is replaced by the thickness of the postshocked gas, relations (2) and (3) are equivalent to equation (A23) of Elmegreen and Lada (1977) except for slight difference in numerical factors by less than a factor of 2.

The quantities T and R appear in relations (2) and (3). We take the minor semidiameter of each ^{13}CO feature as R and the equivalent temperature estimated from the ^{13}CO feature as R

TABLE 4
SUMMARY OF EQUILIBRIUM PARAMETERS OF ^{13}CO FEATURES

Feature	T_{eq}^a (K)	T_{kin} (K)	R^b (pc)	$P_{\text{ext, max}}^c$ ($\times 10^{-10}$ dyn cm $^{-2}$)	$P_{\text{ext}}(\text{H II})^d$ ($\times 10^{-10}$ dyn cm $^{-2}$)	$N_{\text{max}}(\text{H}_2)^e$ ($\times 10^{22}$ cm $^{-2}$)	$N(\text{H}_2)$ ($\times 10^{22}$ cm $^{-2}$)
C1	300	33	0.07 ^f	90.0	28.0	29.0	3.8
C2	170	45	0.07 ^f	28.0	28.0	16.0	4.6
C3	390	60	0.07 ^f	150.0	28.0	37.0	7.0
C4	170	18	0.2	3.2	2.8	3.8	1.2
E1	97	20	0.25	0.75	2.8	2.6	0.75
E2	130	20	0.3	0.94	2.8	2.8	0.53
E3	35	30	0.3	0.068	2.8	0.78	0.89
E4	160	25	0.2	3.2	2.8	5.4	1.5
E5	170	27	0.3	1.6	2.8	3.9	0.94
E6	63	18	0.3	0.22	2.8	1.4	0.25
E8	230	30	0.4	1.7	2.8	3.8	1.1

^a $T_{\text{eq}} = m(\Delta v)^2/8 \ln 2$, m : mean molecular weight. T_{eq} includes contribution from both turbulence and thermal motion.

^b R : a minor semidiameter of ^{13}CO feature.

^c Maximum external pressure under which equilibrium of ^{13}CO feature is possible.

^d Estimated for typical parameters of the H II region.

^e Maximum column density with which ^{13}CO feature is stable if equilibrium is possible.

^f Assumed. See the text.

and the equivalent temperature estimated from the ^{13}CO line width as T . T appears to be accurately determined from the ^{13}CO line width. On the other hand, R may be suffering from larger uncertainties than T and can importantly influence the present analysis. If we, for instance, overestimate R , $P_{\text{ext, max}}$ is underestimated and we may erroneously find that even a stable ^{13}CO feature is gravitationally unstable according to relation (2). $P_{\text{ext, max}}$ is proportional to the square of R , and we should be cautious against overestimating R . In order to avoid this sort of error, we take the minor semidiameter as R . Further, the present beam size, 2.7, may not be small enough to resolve actual sizes of some of the ^{13}CO features. In fact, in equi-velocity diagrams (Fig. 4), we see that the intensity peaks of C1, C2, and C3 are not sufficiently resolved with the present beam. The high angular resolution data taken with a $\sim 1'$ beam size show that the minor diameters of C1, C2, and C3 are about 0.15 pc (Schloerb, Goldsmith, and Scoville 1982; Schloerb and Loren 1982). Therefore, we assume $R = 0.07$ pc for C1–C3. Features C4 and E1–E8 do not appear to be seriously under-resolved in Figures 4 and 8, and we adopt the estimates in Table 2 to calculate $P_{\text{ext, max}}$ and $N_{\text{max}}(\text{H}_2)$. Influence due to projection will be discussed in individual cases.

Another parameter we should estimate is the pressure of the H II region. Features C1–C3 are located in the central part of the H II region, and most of them appear strongly interacting with it. Here we take $n_e = 10^3 \text{ cm}^{-3}$ and $T_e = 10^4$ K for the H II region facing C1–C3 (cf. Goudis 1982). Then, we obtain $P_{\text{ext}} = 2.8 \times 10^{-9} \text{ dyn cm}^{-2}$. Features C4, E1–E6, and E8 are located toward the less bright part of the H II region than C1–C3, and are probably interacting with the H II region more weakly than C1–C3. If we assume $n_e = 10^2 \text{ cm}^{-3}$, and $T_e = 10^4$ K for the periphery of the H II region (cf. Goudis 1982), we obtain $P_{\text{ext}} = 2.8 \times 10^{-10} \text{ dyn cm}^{-2}$. Table 4 summarizes results of calculations of $P_{\text{ext, max}}$, $N_{\text{max}}(\text{H}_2)$, and P_{ext} . We note that the assumption that the external pressure is isotropic also helps to avoid overestimating the degree of instability.

In Table 4, we see that for the ^{13}CO features other than E3 and E6 P_{ext} is either smaller or 2–4 times larger than $P_{\text{ext, max}}$. When we take account of the crudeness of the present estimates, factors of 2–4 do not strongly argue for gravitational instability. If we take account of other forces like rotation or magnetic pressure which are neglected in the above, the stability of the ^{13}CO features increases even more. $N(\text{H}_2)$ is smaller than $N_{\text{max}}(\text{H}_2)$ for these features. Therefore, we conclude that most of the ^{13}CO features are nearly in stable dynamical equilibrium.

On the other hand, E3 and E6 have $P_{\text{ext, max}}$ smaller than P_{ext} by factors of 41 and 13, respectively. Does this imply that they are actually gravitationally unstable? We consider that E3 and E6 can be gravitationally unstable provided that their actual thicknesses are close to what are observed. The greatest ambiguity probably lies in determining R . If we are not looking at the two ^{13}CO features right from their edges, projected sizes of the clouds become significantly larger than actual thicknesses. We note that E3 can be stabilized, if the actual thickness $2R$ is $\lesssim 1/(41)^{1/2} \approx$ one-sixth of the present value, i.e., $\lesssim 0.1$ pc ($= 40''$). When we use the molecular column density of E3, $9 \times 10^{21} \text{ cm}^{-2}$, and the thickness 0.1 pc, we obtain average volume density of $\sim 3 \times 10^4 \text{ cm}^{-3}$ in E3. This density is not unreasonably high and may, in fact, be consistent with the detection of weak HCN and $\text{HCO}^+(J = 1-0)$ emission ($T_R^* \approx 0.5$ K) toward E3 with the 4 m telescope (Sugitani 1985, private communication). If such a small thickness of ~ 0.1 pc is actual

for E3, E3 can be stabilized by the observed line width of $\sim 0.9 \text{ km s}^{-1}$. In this context, better determination of density of E3 is highly interesting. Another possibility for stabilizing E3 is rotation or other systematic motion against contraction. These effects, however, do not seem significant because the peak velocity and line width are remarkably uniform throughout E3 as shown in Figure 9. There is as yet no observational information concerning the magnetic field in E3 in spite of the potential importance of the magnetic pressure. A similar argument is applicable to E6. We find that E6 can be stabilized if the actual thickness of E6 is $\lesssim 1/(13)^{1/2} \times 0.6 \text{ pc} \approx 0.2 \text{ pc}$. This thickness is reconciled with the observed size if E6 is a molecular sheet which is moderately inclined to the line of sight.

b) Discussion

H II expansion is considered to be effective in triggering star formation in interstellar molecular clouds. Among all, the Orion region is discussed as one of the most typical examples in which H II triggering of star formation is important (e.g., Elmegreen and Lada 1977). The present data indicate the molecular features which are directly interacting with H II region. The results of our analysis show that most of the molecular features are nearly in stable equilibrium, and that two of them which are located at the southern edge of the H II region can be gravitationally unstable if their thicknesses are close to what are observed. What are the implications of the present conclusions on H II triggering of star formation?

Gravitational stability of molecular gas compressed by the H II expansion is investigated by Elmegreen and Lada (1977). Their model predicts that a shock-compressed layer driven by an OB subgroup becomes gravitationally unstable after the layer travels over 10–20 pc, or after $\sim 2 \times 10^6$ yr, to form another OB subgroup. The Trapezium stars have an age of $\sim 3 \times 10^6$ yr (Blaauw 1964), which appears sufficiently large for a shock compressed layer to become unstable. The observed molecular column densities $\gtrsim 10^{22} \text{ cm}^{-2}$ of the ^{13}CO features also seem sufficiently large for the layers to become unstable.

We note that C2 shows signs of recently formed stars, the KL/BN objects. The enormous infrared luminosity of the KL/BN objects $\sim 10^5 L_\odot$ suggests that they represent a cluster of recently formed massive stars (e.g., cf. Goudis 1982 and references therein). Their ages are, however, not clearly known, and the stars may be of the same generation as the Trapezium stars. Therefore, one cannot say that the formation of KL/BN objects is triggered by the Orion H II region. The feature C2 shows a ^{13}CO line width which is large enough for supporting against gravity and the H II pressure. The internal motion in C2 may be enhanced by the outflowing gas driven by the infrared cluster.

What will happen to the other molecular features which appear nearly in stable equilibrium at present? Will they acquire more mass so as to become unstable soon? This is, however, not very likely because the present ^{13}CO map shows that most of the molecular mass is already concentrated in the present molecular features and one cannot expect that the molecular features can accumulate molecular gas whose column density is significantly greater than the present value.

We speculate that the cloud internal motion determining the ^{13}CO line width may be one of the key parameters which initiate gravitational instability. This is suggested by the observation that the farthest features E3 and E6 appear most unstable. As is found in Table 2, the two features are character-

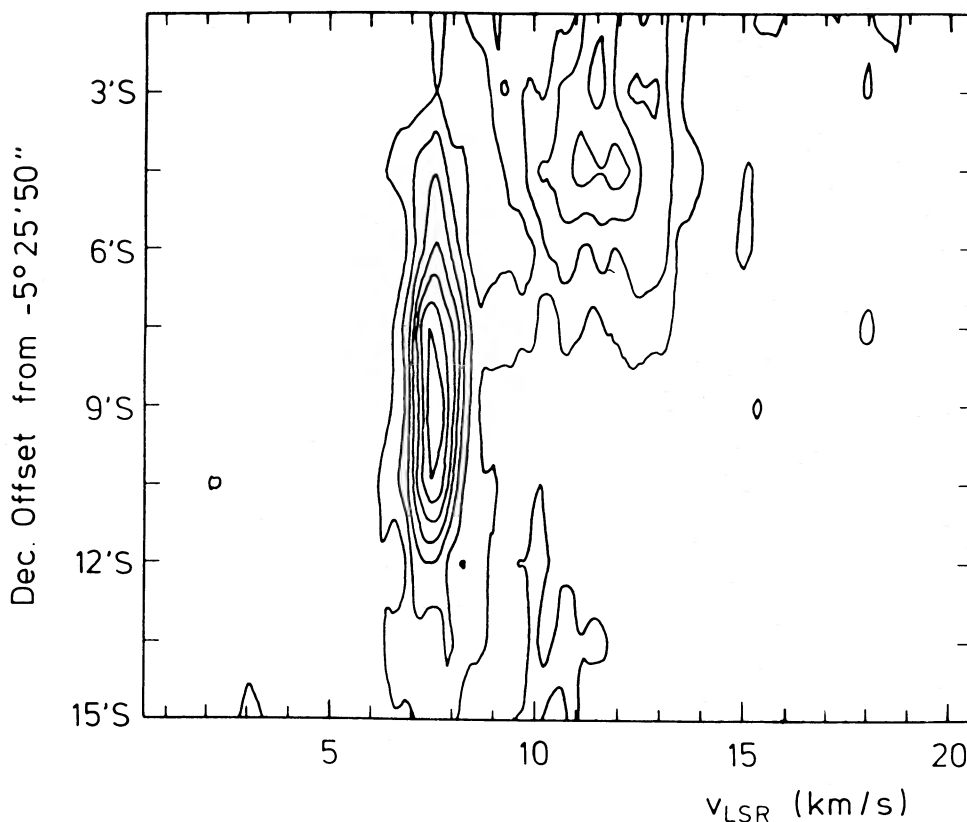


FIG. 9.—Velocity-position map of the ^{13}CO feature E3. Contour unit and the lowest contour are 1 K. R.A. = $5^{\text{h}}33^{\text{m}}29^{\text{s}}.0$.

ized by the smallest ^{13}CO line width around 1 km s^{-1} and are located at the greatest distance from the exciting stars. The internal motion of the central molecular features which are strongly interacting with the H II region is probably subject to strong disturbance due to ionization/shock fronts. On the other hand, the molecular features more weakly interacting with the H II gas can have smaller line widths. Because the internal pressure of the molecular features is proportional to $(\Delta v)^2$, such enhancement of internal turbulence may effectively regulate the gravitational stability, explaining, at least in part, the trend of gravitational stability found in the ^{13}CO features.

VII. SUMMARY

We have observed $J = 1-0$ lines of ^{13}CO and CO in Orion A (M42) to study the distribution, kinematics, and gravitational stability of molecular clouds. The main results of our study can be summarized as follows:

1. In this region, we discern two main ridges and 14 separate features: C1–C4, which are within 1 pc of the Trapezium stars; E1–E8, the West Protrusions, and the West Rim, which are extended by $\sim 4 \text{ pc} \times \sim 4 \text{ pc}$. Most of the molecular features toward the Orion Nebula are interacting with the H II region. In particular, C1–C3 appear to be interacting strongly with the H II region.

2. Evidence is presented that C1–C4 form a molecular

cavity of radius $\sim 0.6 \text{ pc}$ around the Trapezium stars. This cavity is most likely produced by the ionization of the Trapezium stars and/or expansion of the H II region.

3. Some of the extended features, E2, E3, E5, E8, the West Protrusions, and the West Rim, correspond well to the optical features and are likely located at the interface with the H II region. E2, E3, E5, and E8 probably halt the H II expansion, causing an asymmetric expansion of the Orion Nebula.

4. It is not clear if the ^{13}CO features identified represent swept-up material due to the H II region; in some cases, we find that initial inhomogeneities of the undisturbed cloud can better explain the molecular distribution.

5. We tested the gravitational stability of the ^{13}CO features by applying the virial theorem and find that most of the features are nearly in stable equilibrium.

6. Narrowly, E3 and E6 can be gravitationally unstable provided that their actual thicknesses are close to what are observed.

We thank Professor K. Ishida of Kiso Observatory for kindly permitting us to use the photograph of H α emission. Comments by the referee were very helpful in clarifying the latter part of this paper. This work was financially supported by the Grants-in-Aid for Scientific Research of the Ministry of Education, Science, and Culture of Japan (56420004, 57420003, 58420004, and 59420002).

APPENDIX

THE EXTENDED ¹³CO EMISSION

We show integrated intensity maps of ¹³CO (Figs. 8a, 8b, and 8d) superposed on the photograph of H α emission, and Figure 8c. We find that the extended emission has a complicated distribution as a whole, but on each panel at different velocities we can discern separate ¹³CO features in the extended emission. We refer to them as E1 through E8, "the West Protrusion," and "the West Rim." In the following, we shall describe each of them. They include two features which lie within the 1 pc of the center. These features in a schematic drawing (Fig. 7) are listed in Table 1, as well as remarks on optical features of [S II] and [N II]. In Figure 8, it is also seen that the main ridge consists of two components; the northern main ridge at V_{LSR} about 10 km s⁻¹ and the southern main ridge at V_{LSR} about 8 km s⁻¹. The Trapezium stars and the BN/KL infrared objects appear located roughly at a point of contact of the two components.

I. E1

A feature (E1) peaked at (0', 7.5S) is seen toward the main ridge. Although this is not located at the border of the optical nebula, the large blueshift of about 3 km s⁻¹ and its narrow spike like line shape of about 1.5 km s⁻¹ suggest that this feature is not part of the quiescent southern main ridge but is dynamically influenced by the H II regions as suggested by Goldsmith *et al.* (1982).

II. E2

A feature (E2) peaked at (4.5E, 4.5N) is found to be located toward 3' north of the optical dark bay (Fig. 8a). The feature extended toward the dark bay and may be responsible for the heavy obscuration in that direction.

III. E3

A feature (E3) appears at (9'E, 9'S). This is elongated along the east rim of the optical emission (Fig. 8a), where [S II] filaments are seen (Gull 1974). Its spectral line shape is spike-like with extremely narrow line width of about 0.9 km s⁻¹, and its peak velocity is remarkably uniform at 7.5 km s⁻¹ (Fig. 9).

IV. WEST PROTRUSIONS

The West Protrusions are seen toward (9'W, 9'S), which looks like a protrusion toward the northwest from the main ridge (Figs. 8a and 8b). The protrusive features occur between 6.5 and 10.5 km s⁻¹ at spatially shifted locations. Although it is not clear that they are actually located at the rim of the optical nebula because the southern nebula boundary is not well defined, their morphology suggests they face the expanding H II region and have been influenced by it. Measurements of [N II] emission indicate the ionized gas has a component at LSR velocities of 7 to 10 km s⁻¹ toward the protrusive features (Goudis *et al.* 1984), suggesting the association.

V. E4

A slightly protrusive feature toward the west appears on the northwest of C1 (Fig. 8a). This feature (E4) continues up to 9.5 km s⁻¹ and is noticed by Loren (1979). This is probably associated with the northern rim of the optical nebula as suggested by Loren (1979). The interaction of E4 with the H II region is evidenced by [S II] northern rim (Gull 1974).

VI. WEST RIM

At (12'W, 0') a thin ridge extends toward the north. At this right ascension, we find ¹³CO features which are elongated in a north-south direction at velocities through 7.5–11.5 km s⁻¹ (Figs. 8a–8c). Their peak intensities are weak but they appear as a significant straight ridge about 20' in length in the integrated intensity map (Fig. 3). Part of this ¹³CO ridge is seen in a CO($J = 1-0$) map at $V_{\text{LSR}} = 10.5$ km s⁻¹ by Loren (1979). Toward this feature, several [S II] filaments are known to occur at the declination range from 8'S to 2'N ("West Rim" features by Gull 1974) and the [N II] emission has the same LSR velocity of 7 km s⁻¹ (Goudis *et al.* 1984). This declination range is similar to that of the ¹³CO feature at 8 km s⁻¹. Therefore, the ¹³CO features are likely interacting with the optical nebula. We find that the west rim has a velocity gradient in the north-south direction.

VII. E5

A feature (E5) occurs at 1.5N and from 3'E to 15'E (Fig. 8b). This is beyond the northern boundary of the optical nebula, and there is no evidence for interaction with the H II region.

VIII. E6

From the southern main ridge at about 18'S extend two protrusive features toward the east and the northwest, respectively (Fig. 8b). The eastern one is E6. Although E6 is not associated with the clear boundary of the optical nebula, its morphology suggests that it is interacting with the expanding H II region. At present, there is no optical velocity data available for E6.

IX. E7

A protrusion (E7) occurs to the west of the northern main ridge (Figs. 8c and 8d). This is located about 4' north beyond the northern rim of the optical nebula.

X. E8

A feature (E8) appears at 6'E in right ascension and from 3'N through 6'S in declination. This is located at the northern rim of the optical nebula (Figs. 8c and 8d) and is very likely interacting with the H II region. As noticed in Figure 6c, this seems to be kinematically continuous with the bright bar feature. This is a part of the CO expanding ring suggested by Loren (1979).

REFERENCES

- Akabane, K., Sofue, Y., Hirabayashi, H., Inoue, M., Nakai, N., and Handa, T. 1985, *Pub. Astr. Soc. Japan*, **37**, 123.
 Blaauw, A. 1964, *Ann. Rev. Astr. Ap.*, **2**, 213.
 Bodenheimer, P., and Tenorio-Tagle, G. 1979, *Ap. J.*, **233**, 85.
 Dickman, R. L. 1978, *Ap. J. Suppl.*, **37**, 407.
 Draine, B. T., and Roberge, W. G. 1984, *Ap. J.*, **282**, 491.
 Elmegreen, B. G., and Lada, C. J. 1977, *Ap. J.*, **214**, 725.
 Goldsmith, P. F., Arquilla, R., Schloerb, F. P., and Scoville, N. Z. 1982, in *Regions of Recent Star Formation*, ed. R. S. Roger and P. E. Dewdney (Dordrecht: Reidel), p. 295.
 Goudis, C., ed. 1982, *The Orion Complex: A Case Study of Interstellar Matter* (Dordrecht: Reidel).
 Goudis, C., Hippelein, H. H., Meaburn, J., and Songsathaporn, R. 1984, *Astr. Ap.*, **137**, 275.

- Gull, T. R. 1974, in *Proc. ESLAB Symposium on H II Regions and the Galactic Center*, ed. A. F. Moorwood (ESRO SP-105).
- Jaffe, D. T., and Pankonin, V. 1978, *Ap. J.*, **226**, 869.
- Johnston, K. J., Palmer, P., Wilson, T. L., and Bieging, J. H. 1983, *Ap. J. (Letters)*, **271**, L89.
- Kawabata, K., Ogawa, H., Fukui, Y., Takano, T., Fujimoto, Y., Kawabe, R., Sugitani, K., and Takaba, H. 1985, *Astr. Ap.*, in press.
- Loren, R. B. 1979, *Ap. J. (Letters)*, **234**, L207.
- Pankonin, V., Walmsley, C. M., and Harwit, M. 1979, *Astr. Ap.*, **75**, 34.
- Schloerb, F. P., Goldsmith, P. F., and Scoville, N. Z. 1982, in *Regions of Recent Star Formation*, ed. R. S. Roger and P. E. Dewdney (Dordrecht: Reidel), p. 439.
- Schloerb, F. P., and Loren, R. B. 1982, in *Symposium on the Orion Nebula to Honor Henry Draper*, ed. A. E. Glassgold, P. J. Huggins, and E. L. Shuckin, *Ann. NY Acad. Sci.*, **395**, 32.
- Spitzer, L. 1978, *Physical Processes in the Interstellar Medium* (New York: John Wiley and Sons).
- Takano, T., et al. 1983, *Pub. Astr. Soc. Japan*, **35**, 323.
- Tenorio-Tagle, G. 1979, *Astr. Ap.*, **71**, 59.
- Wilson, T. L., and Pauls, T. 1984, *Astr. Ap.*, **138**, 225.

Y. FUKUI, K. KAWABATA, H. OGAWA, and K. SUGITANI: Department of Astrophysics, Nagoya University, Chikusa-ku, Nagoya 464, Japan

COMPACT RADIO SOURCES ASSOCIATED WITH MOLECULAR OUTFLOWS

RONALD L. SNELL

Five College Radio Astronomy Observatory, University of Massachusetts, Amherst

AND

JOHN BALLY

AT&T Bell Laboratories, Holmdel, New Jersey

Received 1985 April 8; accepted 1985 October 7

ABSTRACT

We report the detection of compact radio continuum sources from 12 regions containing molecular outflows. All infrared sources associated with these outflows having a bolometric luminosity in excess of $100 L_{\odot}$ were detected; in addition, three infrared sources with bolometric luminosities under $100 L_{\odot}$ were also seen. Out of seven sources for which spectral indices were determined, three sources have a spectral index near 0.7, indicating an ionized, spherical outflow at constant velocity. The remaining sources exhibit flat spectra indicative of optically thin, thermal emission. For all sources, if the radio emission is formed by a steady, fully ionized wind, the implied mass loss parameters fail by one or two orders of magnitude to explain the energetics of the associated molecular outflows.

We have made detailed, high-resolution radio maps toward two clusters of luminous ($L_{\text{bol}} > 10^3 L_{\odot}$) infrared sources near NGC 2071 and S255. Each cluster consists of three compact sources with typical separations of roughly 10^{17} cm, similar to the size of the Trapezium in Orion. The parameters of the three sources in NGC 2071 suggests that the radio emission originates in a region with solar system-sized dimensions and electron densities $n_e > 10^4 \text{ cm}^{-3}$.

We also present 1.4 GHz maps of the extended H II regions S254, S255, S257, and S187, which are located near molecular outflows. S187 contains a central cavity which exhibits limb brightening. This may be a relic of the stellar wind bubble which has cleared the central part of the H II region.

Subject headings: infrared: sources — interstellar: molecules — nebulae: H II regions

I. INTRODUCTION

The birth and early evolution of stars is frequently accompanied by a remarkable episode of energetic mass outflow revealed by the presence of broad molecular emission lines, high-velocity masers, near-infrared emission of shock-excited H_2 molecules, and high-velocity Herbig-Haro objects. The distribution of high-velocity gas in many regions appears bipolar, indicating outflow along an axis of symmetry (Bally and Lada 1983; Edwards and Snell 1984). Most molecular outflows are associated with highly obscured infrared sources. Although the details of the mechanism responsible for the outflows remain a mystery, those buried objects are probably the ultimate source of a stellar wind that provides the momentum and energy for the molecular outflows. These objects have a wide range of bolometric luminosity: the most luminous objects, such as DR 21 (Fischer *et al.* 1985), Orion (Kwan and Scoville 1976), and Cep A (Rodríguez, Ho, and Moran 1980), have luminosities in excess of $10^4 L_{\odot}$; while the least luminous objects, such as L1551 IRS 5 (Snell, Loren, and Plambeck 1980), HH 7-11 IR (Snell and Edwards 1981), and T Tauri (Edwards and Snell 1982), have luminosities less than $100 L_{\odot}$.

Many of the infrared objects associated with molecular outflows are surrounded by ultracompact radio continuum emission regions (Bally and Predmore 1983; Simon *et al.* 1983; Rodríguez and Canto 1983). Even the low-luminosity objects such as L1551 IRS 5 ($L \approx 38 L_{\odot}$, Emerson *et al.* 1984) exhibit radio continuum emission (Cohen, Bieging, and Schwartz 1982). The Lyman continuum flux emitted by a zero-age main-sequence star with the measured bolometric luminosity is insufficient by several orders of magnitude to maintain in

photoionization equilibrium an H II region of the observed radio flux. Even for intermediate-luminosity infrared objects such as GL 490 and NGC 2071 IR ($L \approx 10^3\text{--}10^4 L_{\odot}$), a discrepancy exists between the available flux of ionizing photons emitted by the central object as estimated from the luminosity and the observed radio flux. This effect becomes even more severe, as shown by Thompson (1982), if one measures the ionizing flux using observations of the infrared recombination lines.

The radio continuum emission generated by these compact sources can be either free-free emission from an ultracompact photoionized H II region or emission from a supersonically expanding ionized stellar wind. These two possibilities might be distinguished either by the morphology of the radio continuum emission or by the shape of the radio spectrum. For a fully ionized stellar wind, the spectrum rises steadily as $S_{\nu} \propto \nu^{\gamma}$, where $\gamma \approx 0.6$ (Panagia and Felli 1975; Wright and Barlow 1975). This spectrum is distinct from that produced by an optically thick H II region ($\gamma = 2.0$) or an optically thin H II region ($\gamma = -0.1$). The difference of the stellar wind spectrum is directly attributable to the radial electron density gradient; in an H II region the density is approximately constant, while in a stellar wind the density falls rapidly with radius. The observed radio spectra of the ionized gas surrounding the young stars T Tauri, LkH α 101, and S106 IR fit the predictions of the stellar wind model (Cohen, Bieging, and Schwartz 1982; Bally, Snell, and Predmore 1983).

In this paper we present the results of a search for radio emission associated with molecular outflows. These observations place limits on the electron density and emission measure of any plasma that may be associated with these regions. Many

compact radio sources were found, some convincingly associated with the infrared sources postulated to be the energy sources for the high-velocity molecular gas. We have measured the radio spectra of many of the detected radio sources, and these data will be used to test the hypothesis that this emission arises in an ionized stellar wind. Data on 12 separate regions containing 15 high-velocity molecular outflows were obtained. We detected 43 compact radio continuum sources; however, many of these are not related to molecular outflows. The stellar mass loss rates derived from the radio continuum data are compared with the values derived from the observations of the molecular gas. On the basis of these data, we suggest that the radio emission detected in some sources may arise in partially ionized stellar winds.

II. OBSERVATIONS

The observations were obtained with the VLA¹ in 1981 February and December and 1983 January, March, and April. The center coordinates of the 12 fields observed are given in Table 1; also given are the sources observed for phase and amplitude calibration and the frequencies observed. These 12 fields contain 15 separate molecular outflows. Data were obtained in the C configuration (5 km array) at frequencies of 1465 MHz (1.4 GHz), 4885 MHz (5 GHz), and 14964 MHz (15 GHz) in most of the fields. Data from Bally and Predmore (1983) in the A configuration (30 km array) for NGC 2071, CRL 961, and S106 were combined with the C-configuration data to provide both high angular resolution and sensitivity to extended structures. Sources and calibrators were observed alternately over as large an hour angle as possible to obtain the best UV-plane

¹ The VLA is a facility of the National Radio Astronomy Observatory, which is operated by Associated Universities, Inc., under contract with the National Science Foundation.

TABLE 1
SUMMARY OF OBSERVATIONS

Region	R.A.(1950)	Decl.(1950)	Calibrator	Frequencies (GHz)
S187	01 ^h 19 ^m 58 ^s .0	+61°33'00".0	0133+476	1.4, 5, 15
NGC 1333	03 25 58.2	+31 05 46.0	0333+321	1.4, 5, 15
L1551	04 28 40.2	+18 01 42.0	0428+205	1.4, 5, 15
NGC 2024	05 39 12.0	-01 56 42.0	0529+075	5
M78	05 43 32.0	-00 14 00.0	0539-057	5
NGC 2071	05 44 30.0	+00 20 46.0	0539-057	1.4, 5, 15
S255	06 09 58.2	+18 00 17.0	0518+165	1.4, 5, 15
CFL 961	06 31 59.0	+04 15 07.0	0723-008	5, 15
S68	18 27 25.0	+01 12 39.0	1821+107	1.4, 5, 15
AS 353A	19 18 08.0	+10 56 21.0	1947+079	5
S106	20 25 33.0	+37 12 30.0	2005+403	1.4, 5, 15
NGC 7129	21 41 47.7	+65 51 03.0	2146+608	5

coverage. The flux density scale was established by observations of 3C 286 at the beginning of each of the observing periods.

Most of the data processing was completed at the VLA site using the standard data reduction programs. The data were CLEANed and maps generated using the AIPS software package. The resolution of the VLA in the C configuration was approximately 0".8, 2".6, and 8".3 at the frequencies of 1.4, 5, and 15 GHz respectively. For the 5 GHz data in which both A- and C-configuration data were combined, the resolution was approximately 0".5.

III. RESULTS

The coordinates, integrated flux densities, and diameters at 5 GHz of all compact radio continuum sources that were found are presented in Table 2. To be included as a detection, the integrated flux density must be at least 3 times the estimated

TABLE 2
SUMMARY OF POSITIONS, FLUX DENSITIES, AND SIZES OF COMPACT RADIO SOURCES DETECTED

SOURCE	R.A.	Decl.	S (mJy)			DIAMETER (5 GHz)
			1.4 GHz	5 GHz	15 GHz	
S187:						
1a	01 ^h 19 ^m 41 ^s .0	61°32'36".9	...	94.2	27 ± 3	1" × 3"
1b	01 19 42.3	61 32 35.2	...	32.9	<6	1 × 2
Total	527 ± 2	132.6
2	01 19 33.9	61 39 10.0	10.7 ± 2.8
NGC 1333:						
1	03 26 15.0	31 05 31.9	8.4 ± 1.8	3.9 ± 0.6	...	<3
2	03 26 05.5	31 08 14.0	<5	0.9 ± 0.3	...	<3
3	03 26 04.7	31 11 41.0	<5	1.0 ± 0.2	...	<3
4	03 25 56.3	31 05 20.0	<5	2.0 ± 0.4	<2	<3
5	03 25 58.0	31 05 48.0	<5	0.8 ± 0.2	<2	<3
6	03 25 56.8	31 04 48.0	<5	0.6 ± 0.1	<2	<3
7	03 25 52.0	31 05 12.0	<5	0.7 ± 0.2	<2	<3
L1551:						
1	04 28 40.2	18 01 42.0	2.8 ± 0.9	4.3 ± 0.5	<4.2	1 × 0.5
2a	04 28 50.4	18 04 20.0	...	1.4 ± 0.3	...	<3
2b	04 28 50.1	18 04 12.0	...	2.6 ± 0.3	...	<3
2c	04 28 49.8	18 04 02.0	...	3.7 ± 0.3	...	<3
Total	40.5 ± 1.5	7.7 ± 0.5
3	04 29 05.5	18 10 36.0	13.6 ± 1.3
4	04 28 46.0	17 57 03.0	23.3 ± 2.1
5	04 28 23.5	17 51 45.0	17.2 ± 1.1
6	04 28 23.5	18 06 57.0	5.8 ± 1.1

TABLE 2—Continued

SOURCE	R.A.	Decl.	S(mJy)			DIAMETER (5 GHz)
			1.4 GHz	5 GHz	15 GHz	
NGC 2024:						
1	05 39 14.3	-01 55 55.0	...	2.8 ± 0.5	...	<0.5
M78:						
1	05 43 24.2	-00 10 39.0	...	1.0 ± 0.2	...	<3
NGC 2071:						
1a	05 44 30.6	00 20 41.0	...	7.9 ± 0.4	9.2 ± 1.4	3×1
1b	05 44 31.2	00 20 49.0	...	0.6 ± 0.1	<2.0	1×0.5
1c	05 44 30.5	00 20 46.0	...	2.2 ± 0.2	2.4 ± 1.2	1
Total	11.7 ± 1.6	16.9 ± 0.3	18.4 ± 4.4	...
2	05 44 35.6	00 21 32.0	<2.2	0.5 ± 0.1	...	<3
3	05 44 33.5	00 28 00.0	62.2 ± 3.7
S255:						
1	06 09 58.2	18 01 16.0	17.5 ± 2.5	27.2 ± 0.6	28.6 ± 2.3	<3
2a	06 09 59.6	17 59 20.0	...	4.5 ± 0.6	...	<3
2b	06 09 59.5	17 59 11.0	...	3.2 ± 0.5	...	<3
2c	06 09 58.6	17 59 14.0	...	4.4 ± 0.7	...	<3
Total	16.6 ± 2.5	16.1 ± 1.7
CRL 961:						
1	06 31 59.1	04 15 10.0	...	0.8 ± 0.2	2.1 ± 1.2	<0.5
2	06 31 59.4	04 15 09.0	...	0.3 ± 0.1	...	<0.5
S68 (Serpens):						
1a	18 27 17.8	01 13 12.5	...	2.7 ± 0.7	...	<3
1b	18 27 17.4	01 13 16.8	...	3.5 ± 0.9	...	<3
1c	18 27 17.2	01 13 20.0	...	3.6 ± 1.0	...	<3
Total	<6	9.5 ± 0.8	10 ± 3	...
2	18 27 25.5	01 10 41.0	<6	0.7 ± 0.2	...	<3
3	18 26 58.1	00 58 51.0	56 ± 14
4	18 27 18.9	01 19 31.0	24 ± 6
5	18 27 02.3	01 13 03.0	8 ± 3
AS 353A:						
1	19 17 50.8	10 55 57.0	...	5.7 ± 1.3	...	<3
2	19 17 57.3	10 50 37.0	...	1.4 ± 0.5	...	<3
S106:						
1	20 25 33.8	37 12 50.0	...	5.4 ± 0.2	12.3 ± 0.9	<0.5
NGC 7129:						
1	21 41 57.3	65 53 09.0	...	0.9 ± 0.3	...	<3
2	21 41 30.6	65 55 08.0	...	1.5 ± 0.3	...	<3

noise determined from blank fields near the suspected source and weighted appropriately by the area integrated. The highest sensitivity is achieved for unresolved sources. In most of the fields observed, maps of the entire primary beam of a single antenna were not made, so that not all sources within the field may be included in Table 1. A total of 34 compact radio sources, or clusters of sources, have been detected, five of which at higher frequencies are resolved into multiple components, making a total of 43 distinct compact radio sources detected. Upper limits quoted in Table 2 were estimated by multiplying the rms flux density in a single beam by three. Multiple frequency data are available for some of the sources, and the radio spectra of these sources have been determined. We have defined the spectral index (γ) as $S_\nu \propto \nu^\gamma$ and have computed this index using the ratio of the 5 GHz to 1.4 GHz flux density ($S_5/S_{1.4}$) and the ratio of the 15 GHz to the 5 GHz flux density (S_{15}/S_5). The results of these calculations are presented in Table 3. Some caution must be applied in the interpretation of the spectral index based on data obtained over a several-year

period, since if the radio sources are variable the spectral index may be incorrect.

Based on the radio spectra, several of the radio sources clearly have a nonthermal spectrum ($\gamma < -0.1$), suggesting that these sources are probable background extragalactic objects. However, Abbot, Bieging, and Churchwell (1984) have detected nonthermal emission from two O stars; therefore not all radio sources with $\gamma < -0.1$ are necessarily background nonstellar objects. The number of background radio sources expected can be estimated, based on the radio source counts at 5 GHz by Bennett *et al.* (1983) and at 1.4 GHz by Condon and Mitchell (1982). With sensitivity to sources with flux densities 0.5 mJy or greater at 5 GHz and 3 mJy or greater at 1.4 GHz one would expect roughly 0.006 sources arcmin⁻² at 5 GHz and 0.009 sources arcmin⁻² at 1.4 GHz. Therefore, for the typical field sizes mapped, one would expect 1–2 background sources at both 1.4 and 5 GHz.

Only 10 of the sources in which the spectral index has been measured have a spectrum consistent with a thermal origin for

TABLE 3
RADIO SPECTRA OF COMPACT SOURCES

SOURCE	SPECTRAL INDEX (γ)	
	$S_5/S_{1.4}$	S_{15}/S_5
S187:		
1a	-1.1
1b	< -1.5
1 Total	-1.1	< -1.2
NGC 1333:		
1	-0.6	...
2	> -1.4	...
3	> -1.3	...
4	> -0.8	< 0.0
5	> -1.5	< 0.8
6	> -1.8	< 1.1
7	> -1.6	< 0.9
L1551:		
1	0.4 ± 0.3	< 0.0
2	-1.4	...
NGC 2071:		
1a	0.1 ± 0.2
1b	< 1.1
1c	0.1 ± 0.5
1 Total	0.3 ± 0.1	0.1 ± 0.2
2	> -1.2	...
S255:		
1	0.4 ± 0.1	0.0 ± 0.1
2 Total	0.0 ± 0.2	...
CRL 961:		
1	0.9 ± 0.6
S68:		
1 Total	> 0.5	0.0 ± 0.3
2	> -1.2	...
S106:		
1	0.7 ± 0.1
LkH α :		
234	1.4 ± 0.4^a

^a Spectral index based on our 5 GHz flux and the 23 GHz flux measured by Bertout and Thum 1982.

their emission. However, most of the sources listed in Table 2 have unknown spectra. Fifteen of the sources have been tentatively identified, based on their position, with known infrared sources, including all ten of the thermal spectrum sources; these identifications are summarized in Table 4. Those radio sources with thermal spectra or that are coincident with infrared sources will be considered as likely radio-emitting stellar sources embedded within the molecular clouds. The 5 GHz flux that we have measured for L1551 IRS 5, NGC 2071 IRS 1 and IRS 2, S106 IRS 4, and CRL 961 are consistent with previous measurements by Cohen, Bieging, and Schwartz (1982) and Bally and Predmore (1983). Thus, these sources are probably not highly variable on time scales of years. Below we present a description of the general properties of each of the regions that has been observed and a more detailed summary of the results of our search for radio continuum emission from those sources suspected of driving the molecular outflows.

a) S187

The H II region S187 is located in a region of moderate obscuration, probably at a distance of ~ 1 kpc as estimated

from the velocity ($V_{\text{LSR}} = -14.5 \text{ km s}^{-1}$) of the associated molecular cloud. An infrared source, located several arcminutes to the south of the H II region at $\alpha(1950) = 01^{\text{h}}20^{\text{m}}15^{\text{s}}.2 (\pm 0^{\text{s}}.7)$, $\delta(1950) = 61^{\circ}33'08'' (\pm 5'')$ was found by Bally (1980) with extremely red colors [$m(K) = 9.98 \text{ mag}$, $m(L) = 6.79 \text{ mag}$, $m(M) = 4.0 \text{ mag}$]. This source is probably the near-infrared counterpart of AFGL 205, [$m(11 \mu\text{m}) = -1.3$, $m(20 \mu\text{m}) = -3.5$] and a bright IRAS source [$\alpha(1950) = 01^{\text{h}}20^{\text{m}}15^{\text{s}}.2$, $\delta(1950) = 61^{\circ}33'10''$] with flux density (in Jy) of $S_{\nu}(12 \mu\text{m}) = 10.47$, $S_{\nu}(25 \mu\text{m}) = 182.3$, $S_{\nu}(60 \mu\text{m}) = 881.4$, and an upper limit at $100 \mu\text{m}$ of 1716 or less. Observations of the $^{12}\text{CO } J = 1-0$ transition revealed a high-velocity outflow 2' to the west of the infrared source (Bally and Lada 1983). Extensive mapping of the flow (Wolf, Bally, and Lada 1985) shows that it is highly confused with a second cloud component but is probably bipolar in the north-south direction and has an extent of $3' \times 8'$, making it one of the largest flows known. The molecular cloud associated with this region extends at least $\frac{1}{2}^{\circ}$ to the north, exhibiting a north-south-oriented ridge with complex kinematics.

The S187 region was observed at 1.4, 5, and 14 GHz, and two compact sources, one north (S187-2) of the extended H II region S187 and a second south (S187-1) of this H II region, were detected. A map of the 1.4 GHz flux density is shown in Figure 1. The extended H II region shows a central cavity with a bright rim surrounding it; an intensity profile through the H II region is presented in Figure 2 and shows this behavior. The source S187-1 was resolved at 5 GHz into two distinct point sources (see Fig. 3), and the spectra of both of these objects is nonthermal. These sources are probably of extragalactic origin. However, for the S187-2 we have observations only at 1.4 GHz; therefore we have no information on the spectrum and consequently the nature of this source. The 1.4 GHz flux that we observed for the extended H II region, S187, is $940 \pm 3 \text{ mJy}$.

b) NGC 1333

High-velocity CO emission has been detected near HH 7-11 (Snell and Edwards 1981) and HH 12 (Edwards and Snell 1983) in the NGC 1333 region. The HH 7-11 outflow is bipolar and is associated with a nearby, low-luminosity infrared source SVS 13 (Strom, Vrba, and Strom 1976) or HH 7-11 IR. The molecular observations show that the bipolar outflow is oriented with the blueshifted high-velocity gas to the southeast of SVS 13 and the redshifted high-velocity gas to the northwest. The Herbig-Haro objects HH 7-11 are associated with the blueshifted high-velocity gas. Three H₂O masers have been found by Haschick *et al.* (1980), one nearly coincident with SVS 13 and a second roughly 0.5 to the southwest of this source. The second source of high-velocity molecular outflow is near HH 12; the source has primarily blueshifted emission, but the redshifted gas is somewhat confused with the HH 7-11 outflow. The exciting star for HH 12 and the source driving the outflow is unknown; several sources have been suggested as likely candidates, but SSS 107, located 2' south of the Herbig-Haro object, is the most likely one (Strom, Strom, and Stocke 1983).

Our radio continuum search revealed seven compact sources, whose properties are summarized in Table 2. This is more than twice the number expected from radio source counts at 5 GHz (Bennett *et al.* 1983), suggesting that many of these sources may be associated with young stellar objects in the NGC 1333 region. The strongest source found, NGC

TABLE 4
IONIZATION OF COMPACT RADIO SOURCES IN MOLECULAR CLOUDS

Source	Identification	Distance (pc)	N_i (s^{-1})	Spectral Type from N_i	L_{Bol} from N_i (L_{\odot})	L_{Bol} Observed (L_{\odot})	Reference
NGC 1333-2	HH 6	350	1×10^{43}	B4	500	...	
NGC 1333-3	SVS 3	350	1×10^{43}	B4	500	180	1
NGC 1333-4	H ₂ O	350	2×10^{43}	B3	700	...	
NGC 1333-5	SVS 13	350	9×10^{42}	B4	400	58	2
L1551-1	IRS 5	160	1×10^{43}	B4	500	38	3
NGC 2024-1	IRS 2	500	6×10^{43}	B3	1100	3800	4
NGC 2071-1a	IRS 1	500	2×10^{44}	B2	2000	...	
NGC 2071-1b	IRS 2	500	1×10^{43}	B4	500	1000	5
NGC 2071-1c	IRS 3	500	5×10^{43}	B3	1000	...	
S255-1	G192.58-0.04	2500	1×10^{46}	B0.5	10000	10000	6
S255-2c	IRS 1	2500	3×10^{45}	B1	6000	...	
S255-2b	IRS 2	2500	2×10^{45}	B1	5000	26000	6
S255-2a	...	2500	3×10^{45}	B1	6000	...	
CRL 961-1	CRL 961	1400	1×10^{44}	B3	1500	5500	7
S68-1a	FIRS 1a	500	6×10^{43}	B3	1100	...	
S68-1b	FIRS 1b	500	8×10^{43}	B3	1200	300	1
S68-1c	FIRS 1c	500	8×10^{43}	B3	1200	...	
S68-2	SVS 4	500	2×10^{43}	B3	700	90	1
S106-1	IRS 4	500	3×10^{44}	B2	2500	14000	8
NGC 7129-1	LkH α 234	1000	8×10^{43}	B3	1200	1200	1

REFERENCES.—(1) Harvey *et al.* 1984. (2) Cohen *et al.* 1984. (3) Emerson *et al.* 1984. (4) Based on data from the IRAS Point Source Catalog. (5) Sargent *et al.* 1981. (6) Jaffe *et al.* 1984. (7) Harvey *et al.* 1977. (8) Harvey *et al.* 1982.

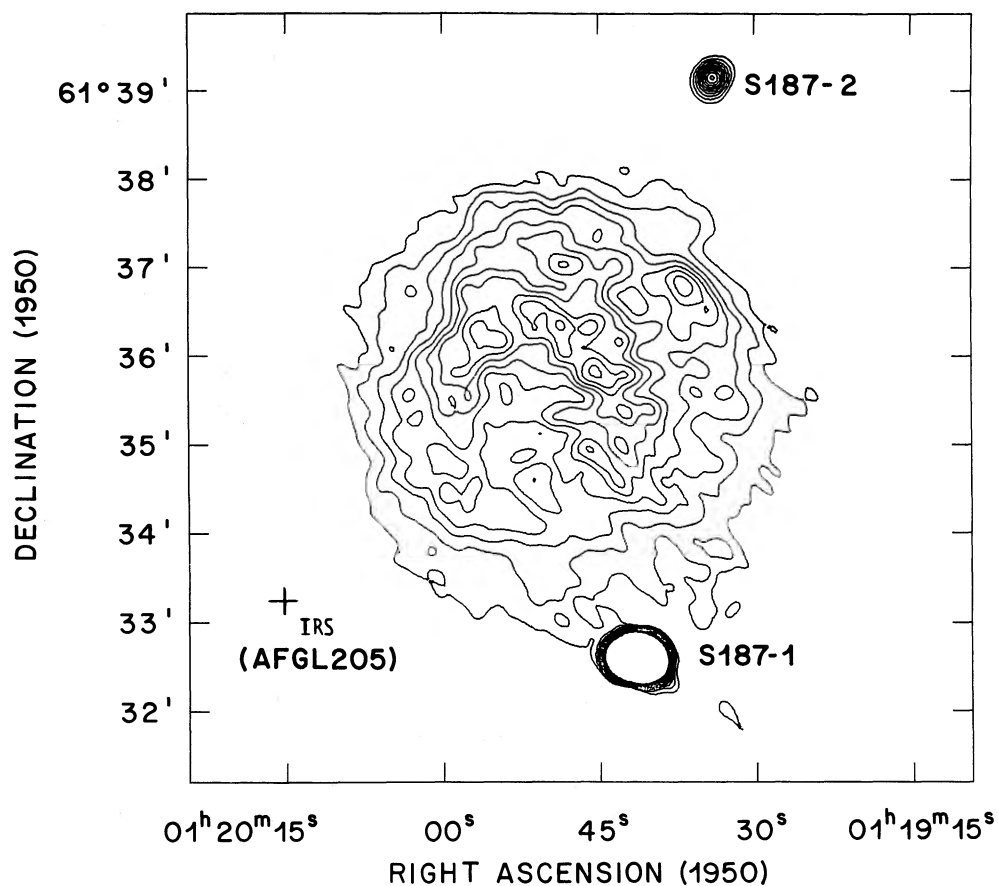


FIG. 1.—1.4 GHz map showing the S187 H II region and two compact radio sources within the field. The plus marks the location of the infrared source discussed in the text. Contour levels are at 1, 2, 3, 4, 5, 6, 7, 8, 9, 10, 11, 12, 13, 14, and 15 mJy per beam.